

The Ly α emission from high- z galaxies hosting strong Damped Ly α systems

Ravi Joshi^{1*}, Raghunathan Srianand¹, Pasquier Noterdaeme² and Patrick Petitjean²

¹*Inter-University Centre for Astronomy and Astrophysics, Post Bag 4, Ganeshkhind, Pune 411007, India*

²*UPMC-CNRS, UMR7095, Institut d'Astrophysique de Paris, F-75014 Paris, France*

Accepted —. Received —; in original form —

ABSTRACT

We study the average Ly α emission associated with high- z strong ($\log N(\text{H I}) \geq 21$) damped Ly α systems (DLAs). We report Ly α luminosities ($L_{\text{Ly}\alpha}$) for the full as well as various sub-samples based on $N(\text{H I})$, z , $(r-i)$ colours of QSOs and rest equivalent width of Si II λ 1526 line (i.e., W_{1526}). For the full sample, we find $L_{\text{Ly}\alpha} < 10^{41} (3\sigma) \text{ erg s}^{-1}$ with a 2.8σ level detection of Ly α emission in the red part of the DLA trough. The $L_{\text{Ly}\alpha}$ is found to be higher for systems with higher W_{1526} with its peak, detected at $\geq 3\sigma$, redshifted by about 300-400 km s⁻¹ with respect to the systemic absorption redshift, as seen in Lyman Break Galaxies (LBGs) and Ly α emitters. A clear signature of a double-hump Ly α profile is seen when we consider $W_{1526} \geq 0.4 \text{ \AA}$ and $(r-i) < 0.05$. Based on the known correlation between metallicity and W_{1526} , we interpret our results in terms of star formation rate (SFR) being higher in high metallicity (mass) galaxies with high velocity fields that facilitates easy Ly α escape. The measured Ly α surface brightness requires local ionizing radiation that is 4 to 10 times stronger than the metagalactic UV background at these redshifts. The relationship between the SFR and surface mass density of atomic gas seen in DLAs is similar to that of local dwarf and metal poor galaxies. We show that the low luminosity galaxies will contribute appreciably to the stacked spectrum if the size-luminosity relation seen for H I at low- z is also present at high- z . Alternatively, large Ly α halos seen around LBGs could also explain our measurements.

Key words: quasars: absorption lines – galaxies: high-redshift – galaxies:ISM – galaxies: star formation

1 INTRODUCTION

Damped Ly α systems (DLAs) are the highest H I column density absorbers seen in QSO spectra, with $N(\text{H I}) \geq 2 \times 10^{20} \text{ cm}^{-2}$. These absorbers trace the bulk of the neutral hydrogen at $2 \leq z \leq 3$ (Prochaska & Wolfe 2009; Noterdaeme et al. 2009, 2012b) and have long been considered to arise from the high-redshift precursors of present day galaxies (for a review see, Wolfe et al. 2005). Presence of enriched elements (Pettini et al. 1994), measured excitation of C II fine-structure levels (Wolfe et al. 2003a; Srianand et al. 2005), existence of a correlation between metallicity and the velocity spread of low-ion absorption lines (Ledoux et al. 2006) akin to the mass metallicity relation seen in galaxies and rotational excitation of high J level of H₂ detected in a

small fraction of DLAs (Ge & Bechtold 1997; Ledoux et al. 2003; Noterdaeme et al. 2008) etc., suggest DLAs are associated in some way with star forming regions. Even if one associates a moderate star formation rate (SFR) to DLAs, they will contribute appreciably to the global inventory of the cosmic star formation rate density at high- z (Wolfe et al. 2003b; Srianand et al. 2005).

A straightforward way to establish the link between the H I gas and stellar components in DLAs is to detect the DLA host galaxies in line or continuum emission. A wide variety of galaxies hosting DLAs are found in imaging studies at low- z (i.e., $z \leq 1$; Chen & Lanzetta 2003; Rao et al. 2003). However, till date only a handful of detections of galaxy counterparts hosting DLAs at $z > 2$ are confirmed using spectroscopy (Möller et al. 2004; Fynbo et al. 2010a; Péroux et al. 2011; Bouché et al. 2012; Fynbo et al. 2010b; Noterdaeme et al.

* E-mail: rjoshi@iucaa.in(RJ)

2012a; Krogager et al. 2012, 2013; Jorgenson & Wolfe 2014; Kashikawa et al. 2014; Rubin et al. 2015; Hartoog et al. 2015; Srianand et al. 2016). Based on all these efforts, the DLAs with emission line detections are found to trace a galaxy population with SFR of $0.4 - 25 \text{ M}_{\odot} \text{ yr}^{-1}$ and impact parameters ranging from $0.4 - 182 \text{ kpc}$, with a mean value of $\sim 25 \text{ kpc}$ (Krogager et al. 2012; Péroux et al. 2011). Christensen et al. (2014) measured stellar masses of these DLA host galaxies. These are found to be consistent with the expected values based on mass-metallicity relations of high- z galaxies. Note, the number of such DLAs are much smaller than the known number of DLAs or galaxies with spectroscopic redshifts. This is mainly because it is found to be challenging as the glare of the bright background quasar makes it difficult to detect the faint galaxy producing the DLA absorption at small impact parameters (Lowenthal et al. 1995; Bunker et al. 1999; Kulkarni et al. 2000, and several unreported attempts).

Issues related to detecting faint galaxies against the glare of a bright quasar can be easily addressed if one can find sightlines with two or more optically thick H I absorbers (Steidel & Hamilton 1992; O’Meara et al. 2006; Christensen et al. 2009; Fumagalli et al. 2010). In these cases the continuum emission from the foreground DLA can be detected at wavelengths less than 912 \AA in the rest frame of the higher redshift optically thick H I absorber that removes the quasar light completely. Using this so called the “Double-DLA” technique Fumagalli et al. (2015) have placed a stringent constraints on the *in-situ* star formation rates, $\text{SFR} < 0.09 - 0.27 \text{ M}_{\odot} \text{ yr}^{-1}$ at the position of the absorbing gas. By looking at the galaxies detected around the QSO sightlines they concluded that most of the DLAs do not originate from highly star-forming galaxies that are coincident with the absorbers.

The effective optical radius of high- z galaxies are small (i.e., $\sim 1 \text{ kpc}$, Shibuya et al. 2015). If we conjecture that the DLAs are associated to such galaxies then the observed number of DLAs per unit redshift requires H I gas to be extended appreciably beyond the stellar regions. Image stacking analysis of high- z galaxies suggests that the stellar distribution is also extended (Hathi et al. 2008; Rafelski et al. 2011). By comparing the covering factor of diffuse emission from Lyman Break Galaxies (LBGs) and H I gas in DLAs (with an assumed star formation efficiency) Rafelski et al. (2011) argued that the star formation in the outskirts of galaxies (i.e., $\sim 6 \text{ kpc}$ from the LBG’s core) may be dominated by atomic gas probed by DLAs with $\log N(\text{H I}) \geq 21$ but with at least a factor 10 less efficiency compared to that seen in local stellar disks. If the framework presented by Rafelski et al. (2011) is true then in a DLA sample of $\log N(\text{H I}) \geq 21$ one should see evidence for low surface star formation along the line-of-sight and a faint galaxy within $\sim 6 \text{ kpc}$. Similarly narrow band image stacking analysis of LBGs at the rest frame Ly α wavelength have shown diffuse Ly α emission extending up to several tens of kpcs (Steidel et al. 2011). In addition, Rauch et al. (2008) have detected a population of faint Ly α emitters with spatially extended Ly α emission that have a total cross-section consistent with that of DLAs. While the Ly α scattering requires only $N(\text{H I}) \geq 2 \times 10^{17} \text{ cm}^{-2}$ to generate large diffuse Ly α emission around LBGs, associating these scattering regions in the LBG’s outskirts to DLAs will also mean that

the low impact parameter regions [that will contribute to the high $N(\text{H I})$ systems (see, Krogager et al. 2012)] can have associated Ly α emission even if there is no *in-situ* star formation being present. All this suggests that the spectral stacking analysis will be very useful in probing DLA-galaxy connection.

Interestingly, in spectroscopic surveys using fibers (e.g., 3 and 2 arcsec diameter fibers employed in SDSS-DR7 and SDSS-DR12 (BOSS), respectively) one integrates, in addition to the light from a distant quasar, the light from all the fore-ground galaxies that happen to fall within the fiber along our line-of-sight. This allows detection of nebular emission lines from such galaxies on top of the QSO spectrum (Wild et al. 2007; Noterdaeme et al. 2010; Ménard et al. 2011; Straka et al. 2015). In this regard, the Ly α emission holds great potential in determining the nature of high- z DLA hosts. Since the direct detections of Ly α emission from high- z galaxies hosting DLAs are very rare, several studies have attempted to detect the Ly α emission in the composite spectra (Rahmani et al. 2010; Noterdaeme et al. 2014). For instance, in a stacking analysis of 341 DLAs of mean redshift $z \sim 2.86$, and $\log N(\text{H I}) \geq 20.62$ seen in the SDSS quasar spectra, Rahmani et al. (2010) have found a 3σ upper limit on SFR of $\leq 1.2 \text{ M}_{\odot} \text{ yr}^{-1}$. Using ~ 95 extremely strong DLAs (ESDLAs) with $\log N(\text{H I}) \geq 21.7$ in the SDSS-DR12 spectra Noterdaeme et al. (2014) have detected the Ly α emission with an average luminosity of $6 \times 10^{41} \text{ erg s}^{-1}$ in the DLA core. These contemporary studies motivate us to unveil the average SFR of DLAs in the stacked spectra by exploiting the unprecedented number of DLAs found in the recent SDSS-BOSS survey (Noterdaeme et al. 2009, 2012b). Note that, this compilation contains ~ 14972 DLA systems with $\log N(\text{H I}) \geq 20.3$ which is a factor of 2.2 larger than the DLA compilation based on SDSS-DR9 by Noterdaeme et al. (2012b). The available information from emission and absorption stacks will not only allow us to detect the Ly α emission but also to probe its dependence on various quantities, such as H I column density, rest equivalent width of metal absorption lines, QSO colors, and absorption redshift.

This article is organized as follows. Section 2 describes our sample selection criteria. In Section 3, we present details of our analysis and average Ly α emission for our full sample and various sub-samples. Section 4 presents discussion based on absorption lines detected in different stacked spectra. In Section 5, we discuss our results in the framework of different possible scenarios. A detailed summary of our study is presented in Section 6. Throughout, we have assumed the flat cosmology with $H_0 = 70 \text{ km s}^{-1} \text{ Mpc}^{-1}$, $\Omega_m = 0.3$ and $\Omega_{\Lambda} = 0.7$.

2 SAMPLE

For our analysis, we have constructed a sample of systems from the BOSS-DR12 DLA catalog, based on automatic search for DLAs in the quasar spectra (see, Noterdaeme et al. 2012b) in SDSS-III BOSS Data Release¹. We use the following stringent criterion: (1) we consider only

¹ <https://www.sdss3.org/>

Table 1. Details of our DLA sample.

Sample	Criteria	DLA systems
Total DLAs	$\log N(\text{H I}) \geq 20.3$	14515
Primary sample	$2.3 \leq z_{\text{abs}} \leq 3.44$ $\text{CNR} \geq 5$ $\log N(\text{H I}) \geq 21.0$ $\beta \geq 5000 \text{ km s}^{-1}$ non-BAL $z_{\text{abs}} > z(\text{Ly}\beta)$	830
New Measurements	$\log N(\text{H I}) < 21.0$ Noisy Spectra Uncertain z Uncertain $N(\text{H I})$	62 8 52 4
Final sample		704

systems with $\log N(\text{H I}) \geq 21.0$. In this case the Ly α absorption has a dark core (with $\tau \geq 10$) spread at least over 7 times the average FWHM ($\sim 160 \text{ km s}^{-1}$) of the instrumental profile of the BOSS spectrograph. (2) We consider DLAs detected in spectra with a median continuum-to-noise ratio (CNR) ≥ 5 . This cut is used to ensure an accurate determination of the H I column density. The CNR is defined over a redshift range with the minimum redshift set redward of any possible Lyman break present in the spectrum and the maximum redshift defined at 5000 km s^{-1} blueward of QSO emission redshift (see also [Noterdaeme et al. 2009](#)). (3) We consider only DLAs that are in the redshift range $2.3 \leq z_{\text{abs}} \leq 3.44$. This redshift range is chosen to avoid the poor signal-to-noise regions in the blue spectrum and to exclude wavelength ranges affected by the residuals from the poorly-subtracted sky emission lines in the red. (4) We restrict ourselves to the observed wavelength range redward of the Ly β + O VI emission line of the quasar to avoid any broad associated O VI absorption being misidentified as a DLA. (5) We avoid DLAs located in the vicinity of the quasar (i.e., the so called proximate DLAs) by considering the systems with velocity offset of $\geq 5000 \text{ km s}^{-1}$ with respect to the quasar emission redshift. After applying these conditions and avoiding sightlines having broad absorption lines from QSO outflows (i.e., BALQSOs), we have a sample of 830 DLAs satisfying the above criterion.

To avoid any uncertainty in the absorption redshift and/or H I column density measurements, we further visually inspected the entire sample and refitted the DLA absorption with a voigt profile. As accurate redshift measurement is critical for detecting the signal in the coadded spectrum, we measure the absorption redshift by cross-correlating the low-ionization metal absorption lines (e.g., C II λ 1334, Si II λ 1526, Al II λ 1670, Fe II λ 1608, 2344, 2374, 2382, 2586, 2600, Mg II λ 2796, 2803) redward to Ly α emission. When no metal absorption line is detected we keep the redshift obtained from the H I Lyman series transitions. This resulted in a final sample of 704 DLA systems with good z_{abs} and $N(\text{H I})$ measurements. Among them, $\sim 80\%$ of the DLAs have redshift determined from metal lines. In the case of 62 DLAs the re-measured $N(\text{H I})$ turns out to be less than our cutoff value 10^{21} cm^{-2} , thereby they go out of our primary sample. Similarly for 64 cases visual inspections, independently by two of the co-authors of this paper,

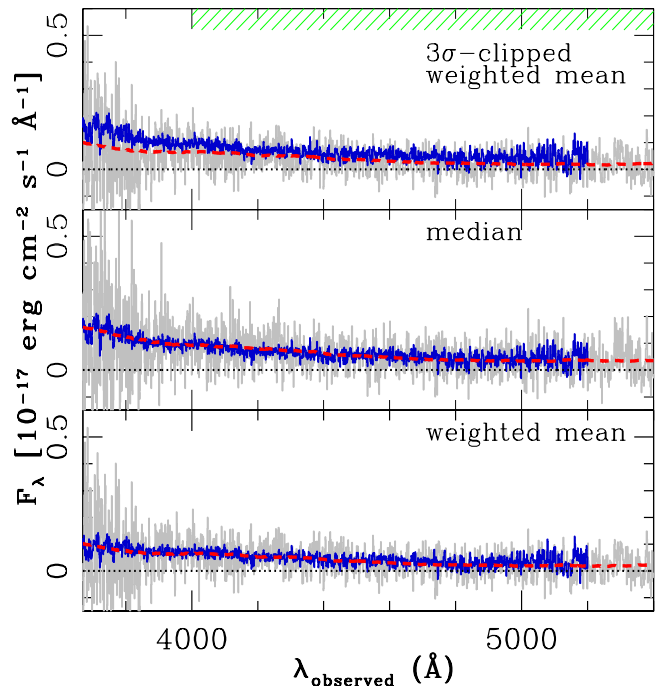


Figure 1. The average residual flux in the Lyman limit region of DLAs (blue solid curve) and in the DLA core pixels with $\tau \geq 10$ (gray curve) are shown as a function of the observed wavelength. The dashed line represents the running average of residual flux in DLA core pixels, which is used as a background template for correcting the residuals in the DLA core. The shaded region in the top panel shows the wavelength range of interest for our stacking analysis.

suggest that the DLA trough is noisy and lack of higher H I Lyman series lines and associated metal lines prevent accurate measurements of $N(\text{H I})$ and z . These 64 systems are also removed from our primary sample. Details of our sample are summarized in Table 1.

While most of the results presented here are based on this sample, sometime to test our results based on smaller sub-samples, in the Appendix we also present result based on samples where we have released the limiting CNR that defines our sample. The reduced one-dimensional spectra for our entire sample of 704 quasars were downloaded from the SDSS-BOSS Data Archive Server². Details about the BOSS spectral information can be found in [Dawson et al. \(2013\)](#). Briefly, the BOSS spectra were obtained with a fiber having a diameter of 2 arcsec (a maximum impact parameter of $\sim 8 \text{ kpc}$ for the above assumed cosmology) and cover a spectral range from $3650 - 10, 400 \text{ \AA}$ at a resolution ($\lambda/\Delta\lambda$) of about $1560 - 2270$ in the blue (i.e., $\lambda \leq 6350 \text{ \AA}$) and $1850 - 2659$ in the red channels.

² <http://dr12.sdss3.org/bulkSpectra>

3 ANALYSIS

3.1 The composite spectra

We have generated several composite spectra with an aim to study both the average emission and absorption properties of high column density DLAs. For stacking, an individual spectrum is shifted to the rest-frame of the DLA, while conserving the flux and rebinning onto a common grid, keeping the same pixel size (constant in velocity space) as the original data (Bolton et al. 2012). We produce the median, continuum normalized stacked spectrum for studying the absorption lines of DLAs. Each individual spectrum is normalized using the best-fit principle component analysis (PCA) continuum model of Bolton et al. (2012). We apply a median-smoothing filter to remove additional imperfections on intermediate scales in the PCA continuum normalized spectra. For this, we mask out pixels possibly containing narrow absorption lines, by only keeping fluctuations within 1.5σ of the continuum. We mainly consider regions redward of the Ly α emission, to avoid the blending by the Ly α forest. The normalized flux error in each pixel of the stacked spectrum is the absolute deviation measured around the mean flux. These spectra are used to study any possible correlation between average absorption properties and the Ly α emission.

For studying the Ly α emission, we convert each spectrum into luminosity per unit wavelength using the luminosity distance at the redshift of the DLAs for the above mentioned cosmological parameters. To remove contribution from any possible outliers, we have used the weighted mean and the 3σ clipped weighted mean statistics with $1/\sigma^2$ weighting with σ being the error in the luminosity. However, we note that using $1/\sigma^2$ weighting will give more weightage to the low redshift systems, when we use the rest frame spectra in luminosity. Therefore, we have constructed the median composite spectrum also. As the DLAs are characterized by a wide flat absorption trough with zero transmitted flux (i.e., dark core), we do not re-scale or normalize the spectrum before the co-addition. The 1σ uncertainty over each pixel in the stacked spectrum is estimated from the central interval encompassing 68% of the flux distribution of the corresponding pixel.

To check and correct the non-zero flux offsets (e.g., see also Rahmani et al. 2010; Cai et al. 2014; Noterdaeme et al. 2014) in the core of DLAs due to poor background subtraction we follow two methods: (i) The average residual flux is calculated by stacking the Lyman limit region (i.e., $\lambda \leq 912 \times (1+z)$ Å) of DLAs in the observer's frame, where the average flux is expected to be negligibly small due to the large expected H I optical depth. For this, we have used 3259 QSO spectra having DLAs in the redshift range $2.95 \leq z \leq 4.6$ whose Lyman limit falls in the observed wavelength range 3600–5100 Å. The stacked spectrum based on three different statistics discussed above are shown in three different panels in Fig. 1 with a blue solid histogram. It is clear that there is a non-zero residual flux present over the redshift range $2.0 \leq z \leq 3.2$ (i.e., $3650 \leq \lambda \leq 5100$ Å) for the Ly α absorption. This residual flux could arise from leakage of far-ultraviolet radiation from the quasar host galaxy through the DLA (Cai et al. 2014) or due to imperfect fiber sky subtraction (Bolton et al. 2012) and should be corrected for before we do the stacking. However, for DLAs in our

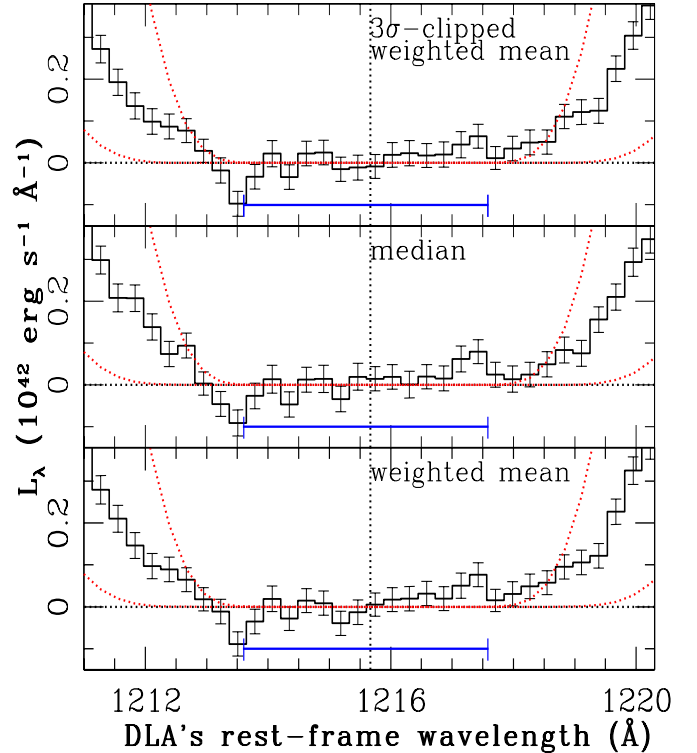


Figure 2. The stacked spectrum corresponds to the 3σ clipped weighted mean (*top*), median (*middle*) and weighted mean (*bottom*), for DLAs in the redshift range of $2.30 \leq z \leq 3.44$. The blue segment shows the DLA core with $\tau \geq 10$ for $\log N(\text{H I}) = 21.0$. The dashed curves show the synthetic profiles for lower (i.e., $\log N(\text{H I}) = 21$) and median (i.e., $\log N(\text{H I}) = 21.23$) column density of DLAs used to get the stacked spectrum.

sample, at $3.2 \leq z \leq 3.4$, we do not have the better residual measurements from the Lyman limit systems. For this z range we use the second method. (ii) We construct the residual flux template (background) by stacking the DLA core pixels with $\tau \geq 10$ that fall within this observed wavelength range. To be specific, we have used the core pixels of all the available DLAs in addition to those that are part of our sample. We generated a template spectrum by considering only the DLA core pixels with optical depth $\tau \geq 10$ for a given $N(\text{H I})$ value. In Fig. 1, we also show the average flux in the stacked spectrum of DLA core regions, constructed using ~ 7072 DLAs with $\log N(\text{H I}) \geq 20.62$ and average CNR ≥ 2 (gray curve). We construct the background for all the three stacking statistics and found that in the overlapping observed wavelength range the residual flux in the Lyman limit region and core of the DLA absorption profile matches well. Besides, we note that the residual flux template does not depend on the brightness and color of the background quasar. Next, in order to account for this average residual flux, we compute its running average (dashed curve) over 300 pixels and constructed the background template for each statistics. We find that the background template obtained by varying the smoothing window in the range of 100–300 pixels gives similar results. Finally, before generating the stacked spectrum in the DLA rest frame, we correct each

spectrum for the non-zero flux offset by subtracting the flux given by the template for the corresponding statistics.

In addition, to the non-zero average flux in the bottom, we also notice in several DLAs there are large pixel-to-pixel variations in the core pixels (see few examples in Fig. A1 in Appendix). While we could associate this with the residual from telluric line subtraction for few cases, the origin of such fluctuations in most cases is unclear. By and large these pixel-to-pixel variations do not affect our results, but may have strong influence when we are dealing with sub-samples having much smaller number of systems. As stated earlier in such cases we relax the CNR constraint that defines our main sample to have additional systems to test the results we get from our main sample.

3.2 The average Ly α emission of DLAs

In Fig 2, we show our stacked spectrum of 704 DLA systems obtained using the weighted mean (*bottom panel*), median (*middle panel*) and 3σ clipped weighted mean (*top panel*) statistics. Our stacked spectra show an asymmetric flux distribution in the bottom of the DLA absorption profile, with a possible enhanced flux in the red half (i.e., $\lambda_r > 1215.67$ Å) within the core region. Such asymmetric Ly α line profiles are naturally produced by the radiative transport of Ly α photons in an outflowing medium (Neufeld 1990, 1991; Verhamme et al. 2006; Hansen & Oh 2006; Dijkstra et al. 2006; Dijkstra 2014).

It is not a straight forward exercise to quantify the Ly α line luminosity (or its upper limit) as the resonant scattering of Ly α photons along with the gas kinematics introduces a wide range of velocity offsets for the escaping Ly α photons. In addition, by stacking, we average over a large number of systems with varied Ly α optical depths and velocity fields. Therefore, we estimate three Ly α luminosities from each stacked spectrum: (i) integrated luminosity over the entire DLA core region, (ii) integrated luminosity (L_λ^b) in the blue part (i.e., core regions having $\lambda_r < 1215$ Å) and (iii) the same (L_λ^r) in the red part (i.e., $\lambda_r > 1215$ Å). We define the core region of the DLA absorption profile to be the wavelength range where the Ly α optical depth, $\tau \geq 10$, for the minimum column density of $\log [N(\text{H I})/\text{cm}^{-2}] \sim 21$ in our sample (see above in Section 2). This is indicated in each panel as a horizontal line. The integrated Ly α luminosity over the DLA core regions are summarized in Table 2. For the full sample, we do not detect any statistically significant signal above the 2σ level. All three statistics give nearly same integrated luminosities and errors suggesting that the stacked spectrum is not severely influenced by few outliers.

Furthermore, to account for the uncertainties related to under/over subtraction of non-zero flux (i.e. background correction) and to test if the stack is influenced by few outliers, we perform a bootstrap analysis. For this, we make stacked spectra of 1000 sub-samples by randomly selecting 90 and 80 per cent of the sample. Note that as we have performed sub-sampling bootstrap with 90% of the sample, the measured statistical error from bootstrap sample is smaller than the uncertainties in each realization (given by the size of the interval including 68% of the pixel value). Therefore, the uncertainty over each pixel is taken to be the maximum error value over 1000 realization.

In this exercise, we also test the presence of any sys-

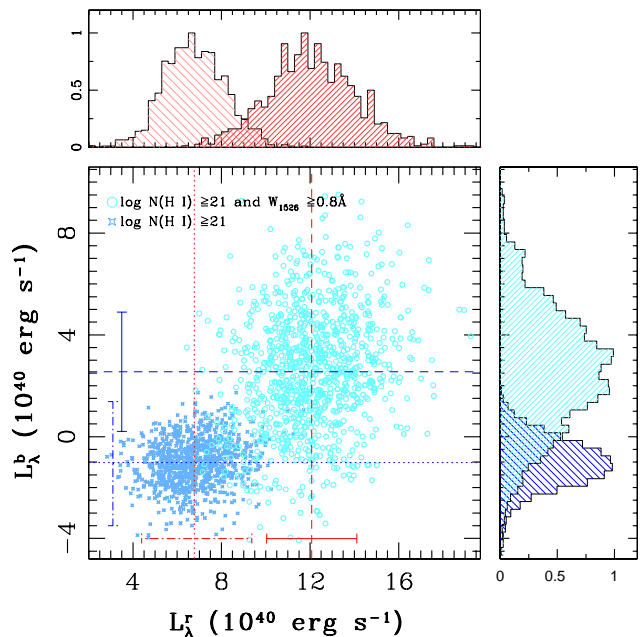


Figure 3. Distribution of the measured mean Ly α luminosities on the red (L_λ^r) and blue (L_λ^b) part of the DLA core region in the bootstrapped stacked spectra for our full sample (*blue star*) and for the sub-sample with $W_{1526} \geq 0.8$ Å (*cyan open circle*), using ~ 1000 random sub-samples generated by considering only 90% size of the sample. The vertical and horizontal (*dashed and dotted*) lines represent the mean bootstrapped luminosity in the red and blue part. The bar shows 1σ deviation of the bootstrap sample around the mean. No correlation is seen between the L_λ^r and L_λ^b , with a Spearman's rank correlation coefficient (r_s) of 0.16 and 0.19, respectively for both the sub-samples. We also show the histogram distribution of L_λ^r and L_λ^b in the figure.

tematic differences between the integrated flux in the blue and red part of the DLA core in the stacked spectra. Results of this bootstrap analysis are summarized in Table 3. Here we consider only the median stacked and 3σ clipped weighted mean spectrum. It is clear from this table that the total integrated luminosity over the core region of the DLA absorption trough are $(5.8 \pm 3.5) \times 10^{40}$ erg s $^{-1}$ and $(5.3 \pm 3.7) \times 10^{40}$ erg s $^{-1}$ respectively when we consider sub-samples with 90 per cent and 80 per cent of the total sample and median stacked spectrum. In Table 3, we also give the Ly α luminosity integrated over the blue and red parts alone. It is clear that, while the luminosity is consistent with zero in the blue part [i.e., $L_\lambda^b = (-1.0 \pm 2.4) \times 10^{40}$ erg s $^{-1}$], there is a 2.8σ excess seen in the red part [i.e., $L_\lambda^r = (6.9 \pm 2.5) \times 10^{40}$ erg s $^{-1}$]. The distribution of the measured luminosities in the blue and red part in individual median stacked spectrum considering 90 per cent of the total sample in each sub-sample is shown with stars in Fig 3. First of all, we note that there is no correlation seen between the Ly α luminosity in red and blue part, with a Spearman's rank correlation coefficient (r_s) of 0.16. It is also clear from the figure that the average Ly α luminosity of the blue part is consistent with zero, whereas, the red part always shows a positive luminosity. From Table 3, we also see this trend being present even when we do bootstrap analysis for 3σ

Table 2. The Ly α line luminosity measured from the stacked spectra.

criteria	number of systems	$\langle \log N(\text{H I}) \rangle$	$\langle z_{\text{abs}} \rangle$	Ly α luminosity ($\times 10^{40} \text{ erg s}^{-1}$)		
				weighted mean	3 σ clipped weighted mean	median
Final sample	704	21.23	2.71	4.54 ± 3.12	4.70 ± 3.19	5.24 ± 3.31
$N(\text{H I}) \geq 10^{21.23} \text{ cm}^{-2}$	354	21.40	2.72	8.83 ± 5.05	9.15 ± 5.13	6.75 ± 5.32
$10^{21} \leq N(\text{H I}) < 10^{21.23} \text{ cm}^{-2}$	350	21.10	2.69	3.06 ± 4.32	3.27 ± 4.36	6.29 ± 4.65
$z_{\text{abs}} \geq 2.7$	352	21.23	2.97	6.21 ± 4.80	6.18 ± 4.78	7.96 ± 5.00
$z_{\text{abs}} < 2.7$	352	21.22	2.48	3.41 ± 4.12	4.60 ± 4.35	3.84 ± 4.39
$W_{1526} \geq 0.8 \text{ \AA}^a$	288	21.25	2.68	10.51 ± 4.95	13.62 ± 5.02	15.82 ± 5.18
$W_{1526} < 0.8 \text{ \AA}$	406	21.26	2.75	4.07 ± 4.67	4.63 ± 4.05	4.71 ± 5.02
$(r - i) \geq 0.1$	352	21.24	2.82	6.22 ± 4.49	5.43 ± 4.56	10.93 ± 4.70
$(r - i) < 0.1$	352	21.22	2.59	3.19 ± 4.34	5.66 ± 4.47	4.02 ± 4.66

^a Only systems with Si II λ 1526 absorption line detection are considered.

clipped weighted mean spectra albeit with slightly lower significance level. *The main conclusion from this section is that the average Ly α luminosity of DLAs with $\log N(\text{H I}) \geq 21$ within 8 kpc to the QSO sightline, is less than one hundredth of the Ly α luminosity of an L $_{\star}$ galaxy (i.e., $L_{\star}(\text{Ly}\alpha) = 5.8 \times 10^{42} \text{ erg s}^{-1}$) at these redshifts (Ouchi et al. 2008). There is a hint of peak emission in the Ly α profile being redshifted with respect to the DLA systemic redshift.*

In what follows, we will explore the dependence of Ly α luminosity on different measurable parameters of the DLA.

3.3 Dependence on $N(\text{H I})$:

The H I column density of DLAs is found to be strongly anti-correlated with the impact parameter of the quasar sightline, where a larger $N(\text{H I})$ typically originates from a sightline with smaller impact parameter (Zwaan et al. 2005; Rao et al. 2011; Péroux et al. 2011; Krogager et al. 2012). In this scenario, we expect the galaxies associated with high H I column density systems to preferably come inside the fiber whereas those associated with low column density will contribute less to the Ly α emission in the fiber spectrum. Recall, that the fiber radius of 1 arcsec corresponds to a physical size of ~ 8 kpc at a median z of 2.7. From figure 8 of Zwaan et al. (2005), we see that a line-of-sight having $\log N(\text{H I}) \geq 21$ will occur, at an impact parameter ≤ 8 kpc, 75 per cent of the times. Whereas, the same for $\log N(\text{H I}) \geq 21.7$ will occur within an impact parameter of 8 kpc in 90 percent of the cases. However, results for high- z DLAs suggest that a given $N(\text{H I})$ could come from a larger impact parameter (see Rao et al. 2011; Péroux et al. 2011) than the one discussed by Zwaan et al. (2005) based on H I emission from low- z galaxies.

On the other hand, Toribio et al. (2011) have found that the size of the H I emitting region in low- z galaxies is proportional to their optical luminosity. Because of this, it is possible that a given H I column density will originate from a large impact parameter for a high luminosity galaxy compared to a low luminosity one. It is also clear from figure 18 in Zwaan et al. (2005) that when we have $\log N(\text{H I}) \geq 21$, at an impact parameter of 10 kpc, the associated galaxy is most likely to be a sub-L $_{\star}$ galaxy. Patra et al. (2013), using H I maps of low- z dwarf galaxies found roughly 10 per cent of the cross-section above $\log N(\text{H I}) = 20.3$ at z

$= 0$ is provided by dwarf galaxies. However, this fraction sharply falls to ≤ 1 per cent by $\log N(\text{H I}) \sim 21.5$ as the cross-section of such gas in dwarf galaxies are very small. Typically these high column density gas are located close to star forming regions even when there is no one to one correspondence between them (Roychowdhury et al. 2014). In this scenario, for our sample with $\log N(\text{H I}) \geq 21$, it is most likely that the stellar light that will directly go through the fiber will come from less luminous galaxies. The brighter galaxies contributing to the absorption likely fall outside the BOSS fiber (López & Chen 2012).

All this motivates us to explore the Ly α emission as a function of the H I column density. In order to understand the dependence of Ly α luminosity on $N(\text{H I})$, we divided the sample into two around $\log N(\text{H I}) = 21.23$, the median $\log N(\text{H I})$ of our sample. The median $\log N(\text{H I})$ of the two sub-samples are 21.1 and 21.4 respectively. The Ly α luminosities measured by integrating over the DLA core region are given in Table 2. For the weighted mean and 3 σ clipped weighted mean the Ly α luminosity measured in the high $N(\text{H I})$ sub-sample is slightly higher than those measured from the low column density sub-sample. However, the difference is not statistically significant considering the associated errors in both measurements. We also note that the measurements based on the median stacked spectrum is similar for both sub-samples. We then consider the bootstrapping results presented in Table 3. As in the case of the whole sample, the Ly α luminosities measured for the red part are always higher than those measured for the blue part. However, even for the red part the difference between two sub-samples based on $N(\text{H I})$ (i.e., $(4.0 \pm 4.9) \times 10^{40} \text{ erg s}^{-1}$ for the median stacked spectrum) are not statistically significant. However, we wish to note here that the range in $N(\text{H I})$ is very small in our sample to reveal any weak trend in the Ly α emission with $N(\text{H I})$.

3.4 Dependence on z :

Next, we consider two sub-samples based on z_{abs} by dividing the full sample at $z_{\text{abs}} = 2.7$. The sub-samples have median redshift of 2.48 and 2.97. From Tables 2, we note that the Ly α luminosity measured over the core region appears to be slightly higher for the high z sample but the difference is not statistically significant. Table 3, also suggests that there is no statistically significant difference in the average Ly α lu-

Table 3. Luminosity of Ly α line in bootstrap analysis for both the median and 3σ clipped weighted mean stacked spectra.

Sample	Ly α luminosity ($\times 10^{40}$ erg s $^{-1}$)			Ly α luminosity ($\times 10^{40}$ erg s $^{-1}$)		
	DLA-bottom	median stack	L_{λ}^r	DLA-bottom	3σ clipped weighted mean	L_{λ}^r
Full with 90% bootstrap	5.82 ± 3.48^a	-1.06 ± 2.44	6.88 ± 2.49	3.87 ± 3.20	-2.27 ± 2.21	6.14 ± 2.32
Full with 80% bootstrap	5.27 ± 3.69	-1.32 ± 2.58	6.58 ± 2.65	3.86 ± 3.40	-2.22 ± 2.35	6.08 ± 2.46
$N(\text{H I}) \geq 10^{21.23} \text{ cm}^{-2}$	6.24 ± 4.95	-2.33 ± 3.46	8.57 ± 3.53	5.58 ± 4.62	-2.51 ± 3.20	8.09 ± 3.33
$10^{21} \leq N(\text{H I}) < 10^{21.23} \text{ cm}^{-2}$	3.55 ± 4.82	-1.00 ± 3.37	4.56 ± 3.45	2.97 ± 4.45	-1.72 ± 3.06	4.69 ± 3.23
$z_{\text{abs}} \geq 2.7$	7.34 ± 5.28	1.72 ± 3.68	5.61 ± 3.79	6.03 ± 4.92	1.17 ± 3.39	4.86 ± 3.57
$z_{\text{abs}} < 2.7$	4.02 ± 4.60	-3.11 ± 3.22	7.13 ± 3.29	2.66 ± 4.27	-4.64 ± 2.96	7.30 ± 3.07
$W_{1526} \geq 0.8 \text{ \AA}^\dagger$	14.55 ± 5.50	2.49 ± 3.87	12.06 ± 3.91	11.33 ± 5.06	2.95 ± 3.51	8.39 ± 3.64
$W_{1526} < 0.8 \text{ \AA}$	0.64 ± 4.55	-3.66 ± 3.15	4.31 ± 3.21	0.80 ± 4.43	-5.20 ± 3.04	5.28 ± 3.22
$W_{1526} \geq 0.4 \text{ \AA}^\dagger$	13.49 ± 4.05	1.16 ± 2.84	12.34 ± 2.90	11.34 ± 3.74	-0.79 ± 2.60	12.13 ± 2.69
$(r-i) \geq 0.1$	9.32 ± 4.97	-0.45 ± 3.56	9.78 ± 3.48	4.84 ± 4.59	-2.57 ± 3.24	7.41 ± 3.24
$(r-i) < 0.1$	3.45 ± 4.93	-0.75 ± 3.36	4.19 ± 3.61	3.42 ± 4.48	-1.59 ± 3.04	5.02 ± 3.30

^a The individual errors are the maximum error seen in the 1000 realization during the bootstrap analysis and not the statistical error of the bootstrap sample.

[†] Only systems with Si II λ 1526 absorption line detection are considered.

minosity as a function of z . As the projected size of the fiber in the whole z range, over which our DLAs are detected, is nearly the same, it does not influence the z evolution. However, in all sub-samples the Ly α luminosity inferred is higher for the red part compared to that of the blue part, albeit with less statistical significance, compared to what we find for the full sample. We note that the smaller z range in our sample provides a limited leverage to reveal any weak trend of Ly α emission with z .

3.5 Dependence on $W_r(\text{Si II}\lambda 1526)$

Prochaska et al. (2008) found a strong correlation between the rest equivalent width of Si II λ 1526 line (denoted as W_{1526}) and metallicity (see also Jorgenson et al. 2013; Neeleman et al. 2013). They found this correlation to be stronger than the correlation found between low ion velocity widths (Δv_{90}) and metallicity (Ledoux et al. 2006). The correlation between W_{1526} and metallicity has also been confirmed by Kaplan et al. (2010) in the case of metal strong DLAs. The measured correlation implies an average metallicity of $Z = -1.48 Z_{\odot}$ (respectively $-1.06 Z_{\odot}$) for $W_{1526} = 0.4 \text{ \AA}$ (respectively 0.8 \AA) with a scatter of 0.25 dex in the metallicity. The average metallicity will be 0.15 dex higher if we use the coefficients found by Jorgenson et al. (2013). As Si II λ 1526 is a strong transition, the absorption line profile will be highly saturated for the high equivalent width systems. Therefore, the measured equivalent width usually samples the velocity field probed by the optically thin gas that is either part of an outflow or in the halo. Thus, this correlation was interpreted as a reflection of the underlying mass-metallicity relation in galaxies (Ledoux et al. 2006; Christensen et al. 2014).

We find the median $W_{1526} = 0.8 \text{ \AA}$, if we consider DLAs with a clear detection of Si II λ 1526 absorption line. Therefore, we consider two sub-samples of DLAs with $W_{1526} < 0.8 \text{ \AA}$ and $\geq 0.8 \text{ \AA}$. The median W_{1526} of these two sub-samples are 0.53 \AA and 1.18 \AA . The DLAs without Si II λ 1526 absorption line detections are also included in the $W_{1526} < 0.8 \text{ \AA}$ sub-sample. From Table 2 (and Fig. 4) we can see that when we consider only systems with $W_{1526} \geq 0.8 \text{ \AA}$

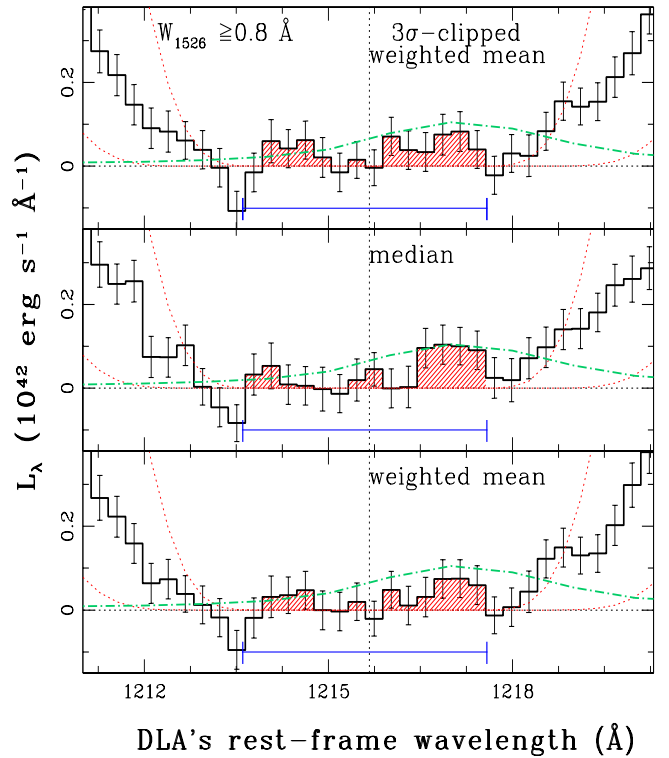


Figure 4. Same as Fig. 2, for the sub-sample with $W_{1526} \geq 0.8 \text{ \AA}$. The dashed curve is Ly α emission in the composite spectrum of LBGs (Shapley et al. 2003) with its amplitude scaled to match the luminosity seen in our stacked spectrum.

the integrated Ly α luminosity over the full DLA core itself is significantly more from zero by more than 3σ level (see Table 2). We find $L = (15.8 \pm 5.2) \times 10^{40} \text{ erg s}^{-1}$, a detection at 3σ level, in the median stacked spectrum. The weighted mean and 3σ clipped weighted mean stacked spectra also show consistent results albeit with slightly less significance. The measured Ly α luminosity in this case corre-

sponds to 2 to 2.5% of the Ly α luminosity of an L $_{\star}$ galaxy at these redshifts. However, for the sub-sample of systems having $W_{1526} < 0.8 \text{ \AA}$, we find $L \simeq (4.7 \pm 5.0) \times 10^{40} \text{ erg s}^{-1}$ in the median stacked spectrum. Consistently lower luminosities are also seen in the case of weighted mean and 3σ clipped weighted mean stacked spectra. The difference in the Ly α luminosities between high and low equivalent width sub-samples is $= (11.1 \pm 7.2) \times 10^{40} \text{ erg s}^{-1}$ for the median stacked spectrum. Therefore, we have a marginal evidence for the Ly α emission being high for high Si II equivalent width systems.

Next, we consider L_{λ}^b and L_{λ}^r for the two sub-samples. For the $W_{1526} \geq 0.8 \text{ \AA}$ sub-sample we find the $L_{\lambda}^r \sim (12.1 \pm 3.9) \times 10^{40} \text{ erg s}^{-1}$ is higher than $L_{\lambda}^b \sim (2.5 \pm 3.9) \times 10^{40} \text{ erg s}^{-1}$ in the median stacked spectrum. The difference, $(9.6 \pm 5.5) \times 10^{40} \text{ erg s}^{-1}$, is significant at a 1.7σ level. The result of bootstrap analysis retaining 90% of the data is also shown in Fig. 3. First of all we notice, unlike the full sample, the scatter is much higher in the W_{1526} based sub-sample. However, it is clear that while there is no statistically significant detection of emission in the blue part, in the red part non-zero fluxes are detected at more than 3σ level. Interestingly, even in the $W_{1526} < 0.8 \text{ \AA}$ sub-sample $L_{\lambda}^r = (4.3 \pm 3.2) \times 10^{40} \text{ erg s}^{-1}$ is stronger than $L_{\lambda}^b = (-3.7 \pm 3.2) \times 10^{40} \text{ erg s}^{-1}$ in the median stacked spectrum. We notice L_{λ}^r in the case of $W_{1526} \geq 0.8 \text{ \AA}$ is higher than L_{λ}^r measured for $W_{1526} < 0.8 \text{ \AA}$ sub-sample with the difference being $(5.1 \pm 5.5) \times 10^{40} \text{ erg s}^{-1}$. As can be seen from Table 3, these trends are also seen when we do the bootstrapping analysis using 3σ clipped weighted mean statistics. However, the difference in the total Ly α luminosity and L_{λ}^r between two sub-samples are weaker when we use 3σ clipped weighted mean stacked spectrum instead of median stacked spectrum. Similar trends are also seen if we consider the results for $CNR \geq 4$ cut-off [see Table A1 in the Appendix]. Furthermore, we have tested the dependence of the strength of the Ly α emission on W_{1526} cut-off by decreasing it to 0.4 \AA and 0.6 \AA and find no strong dependence on this cutoff (see Table A1, Fig. A2).

Results presented here are consistent with Ly α emission being stronger among systems having large W_{1526} . We also note that the distribution of $N(\text{H I})$ and z are similar (see the quoted median values in Table 2) between different sub-samples discussed here purely based on W_{1526} . We discuss the implications of these results in details in the Section 5.

3.6 Dependence of QSO colours:

The general population of DLAs tend to have very little dust so they usually do not cause a strong reddening to the spectra of background QSOs (see Vladilo et al. 2008; Frank & Péroux 2010; Khare et al. 2012; Fukugita & Ménard 2015; Murphy & Bernet 2016). However, due to the resonant nature of the Ly α transition, presence of even a small amount of dust can modify the emerging Ly α line intensity and profile shape. In addition, the spatial distribution of dust can also change the profile of the emerging Ly α emission.

In this section, we study the possible connection between the QSO colour and the stacked Ly α emission. For a given dust content in DLAs the observed color of a QSO at a given redshift will also depend on the absorption redshift.

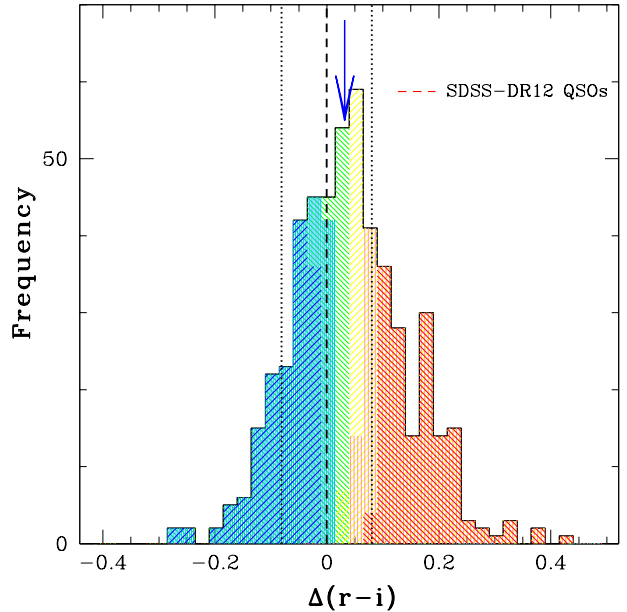


Figure 5. $\Delta(r-i)$ values of the background quasars for the sub-sample with $W_{1526} \geq 0.4 \text{ \AA}$, with a median value is shown with a blue arrow. The $\Delta(r-i)$ distribution for the lower and upper 30, 40, 50% of the sub-samples from $(r-i)$ color distribution are shown with blue, cyan, green, yellow, orange and red color, respectively. The dashed line represents the median $\Delta(r-i)$ color for the SDSS-DR12 QSOs with a similar redshift range of the quasars used in the present work (i.e., $2.38 \leq z_{\text{em}} \leq 3.95$). The dotted lines show the one standard deviation away from that median.

We consider two sub-samples based on $(r-i)$ colour of the QSO.

From Table 2, we see that when we divide our whole sample into two based on $(r-i)$ colours there is no statistically significant difference in the Ly α luminosity between the two sub-samples even though we see slightly higher value of the Ly α luminosity (the difference is only at 1.1σ level) for the redder QSOs when we consider the median stacked spectrum. From Table 3, we also notice that the red part shows a high luminosity of $L_{\lambda}^r = (9.8 \pm 3.5) \times 10^{40} \text{ erg s}^{-1}$ (at $\sim 2.8\sigma$) for the high $(r-i)$ sample. Whereas, the low $(r-i)$ sample show a $L_{\lambda}^r = (4.2 \pm 3.6) \times 10^{40} \text{ erg s}^{-1}$ with an insignificant (only at $\sim 1.2\sigma$) luminosity difference between the two sub-samples. One needs to be careful in interpreting these results as the difference in $(r-i)$ between the two sub-sample is not much and also there is a possible correlation between $(r-i)$ and W_{1526} . Just to explore the role played by the possible presence of dust we restrict our future discussions to systems with $W_{1526} \geq 0.4 \text{ \AA}$. This is because we already have a clear detection of Ly α emission in this case. Thus further dividing sub-sample based on $(r-i)$ is more relevant for probing the connection between reddening and Ly α emission profile.

We compute the $\Delta(r-i)$ colours of QSOs having DLAs in our sample with $W_{1526} \geq 0.4 \text{ \AA}$ by finding the deviation of the $(r-i)$ colour of the QSO with respect to the median $(r-i)$ colour of SDSS-DR12 QSOs at the same redshift. The $\Delta(r-i)$ is found to be strongly correlated with $(r-i)$ with a

Table 4. Ly α luminosity for the sub-sample with $W_{1526} \geq 0.4 \text{ \AA}$ and various $(r-i)$ color-cut.

Sample	$(r-i)$	$\langle \Delta(r-i) \rangle$	Ly α luminosity ($\times 10^{40} \text{ erg s}^{-1}$)			velocity-offset		FWHM (km s^{-1})
			DLA-bottom	L_{λ}^b	L_{λ}^r	Δv^r	Δv^b	
lower 30%	< 0.05	-0.06	22.89 ± 7.21	6.02 ± 4.79	16.87 ± 5.38	298 ± 30	-368 ± 15	196 ± 70
lower 40%	< 0.08	-0.04	21.29 ± 6.38	7.05 ± 4.28	14.23 ± 4.74	336 ± 26	-363 ± 16	144 ± 62
lower 50%	< 0.11	-0.03	14.00 ± 5.82	2.71 ± 3.92	11.29 ± 4.30	272 ± 46	-337 ± 26	214 ± 98
upper 50%	> 0.11	0.10	13.54 ± 5.61	0.34 ± 4.04	13.20 ± 3.89	—	—	—
upper 40%	> 0.13	0.10	20.76 ± 6.24	2.96 ± 4.55	17.80 ± 4.28	—	—	—
upper 30%	> 0.16	0.16	23.15 ± 7.18	6.08 ± 5.37	17.06 ± 4.77	—	—	—

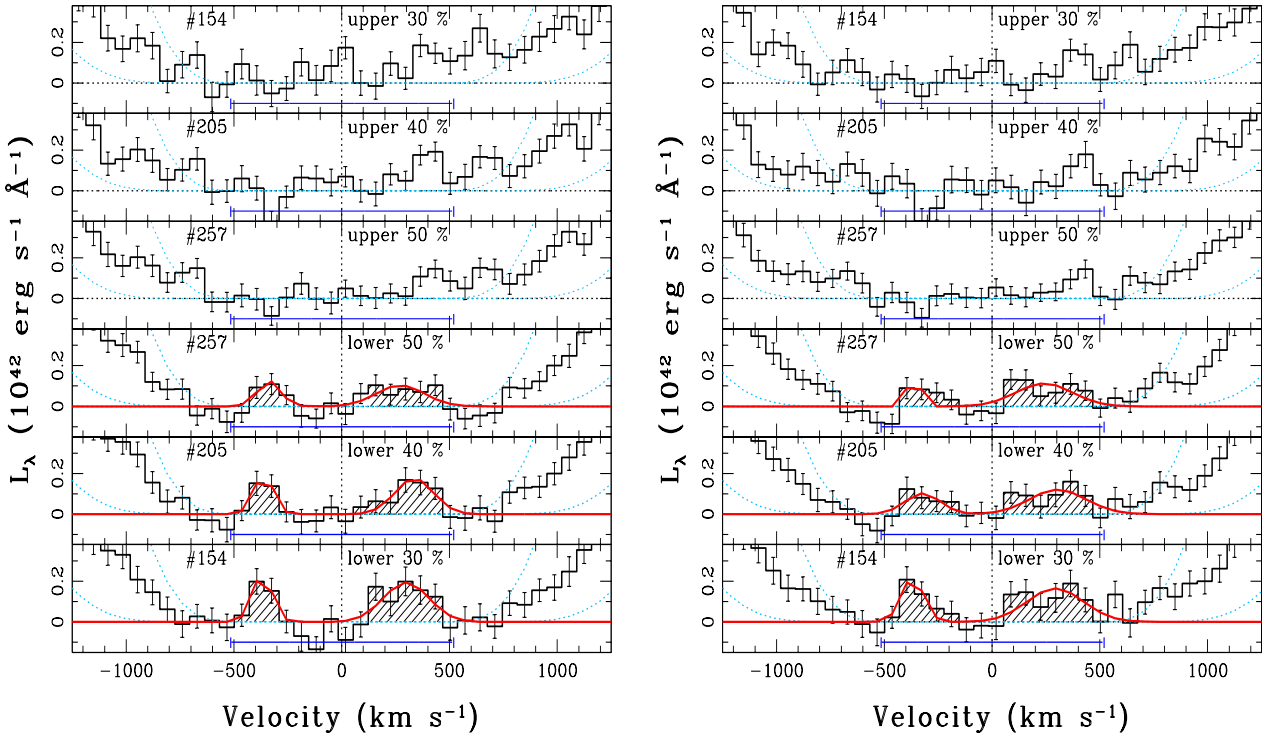


Figure 6. *Left panel (bottom to top)* : The median stacked spectra for various sub-samples with $W_{1526} \geq 0.4 \text{ \AA}$ with color selection criteria of $(r-i) < 0.05, < 0.08, < 0.11, > 0.11, > 0.13,$ and > 0.16 . The blue segment shows the DLA core with $\tau \geq 10$ for $\log N(\text{H I}) = 21.0$. The dashed curves show the synthetic profiles for lower (i.e., $\log N(\text{H I}) = 21$) and median (i.e., $\log N(\text{H I}) = 21.23$) column density of DLAs used to get the stacked spectrum. The solid red curve show the Gaussian fit to the non-zero flux seen in the red and blue part of the DLA core region. *Right panel* : Same as left panel for 3σ clipped weighted mean stacks. See Fig. A3 in the Appendix for results when we consider systems with $\text{CNR} \geq 4$. In each panel the number of DLAs contributing to the plot are also indicated.

r_s of 0.88. In Fig. 5, we show the histogram of $\Delta(r-i)$. The vertical dashed and dotted lines show the median $\Delta(r-i)$ and associated 1σ spread for the general QSOs with the same redshift range of quasars used in the present work. The QSOs in the DLA sample are slightly more redder than the general population of QSOs. The presence of QSOs with negative $\Delta(r-i)$ indicates the possible intrinsic spread in the QSO continuum shape. We divide the $W_{1526} \geq 0.4 \text{ \AA}$ sub-sample into 6 different groups by selecting the lower 30, 40, 50 and upper 50, 40 and 30% DLA systems from the cumulative distribution of measured $(r-i)$ color. Note that, the average W_{1526} for the lower and upper 30% sub-samples are found to be $0.83 \pm 0.13 \text{ \AA}$ and $1.04 \pm 0.16 \text{ \AA}$, respectively. In Table 4, we summarize our results. First six columns summarize the sample, range in $(r-i)$ considered, mean $\Delta(r-i)$ of the group, the total Ly α luminosity, L_{λ}^b

and L_{λ}^r . More information can be obtained from the visual inspection of the profiles given in Fig. 6.

It is clear from Table 4 that when we consider the stacked spectrum of lower 30 per cent of the quasars from $(r-i)$ color distribution, the integrated Ly α luminosity over the full profile is found to be $(22.9 \pm 7.2) \times 10^{40} \text{ erg s}^{-1}$. Unlike all the other cases discussed till now, we do see a clear double hump profile for the Ly α emission in this case (see the bottom panels of Fig. 6). Double hump feature for the lower 30 per cent of the quasars from $(r-i)$ color distribution is also clearly seen even in the 3σ clipped mean stacked spectrum (see right lower most panel in Fig. 6). It is also consistent with the finding of Noterdaeme et al. (2014), where excess Ly α emission is seen in extremely strong DLAs (i.e., $\log N(\text{H I}) \geq 21.7$) with lower $E(B-V)$ (i.e., < 0.025). Results of double Gaussian fit to the observed Ly α profile for

the median stacked spectra are also summarized in Table 4 (see columns 7–9). From Table 4 we notice that in the two low ($r-i$) bins within the measurement errors L_λ^r is twice that of L_λ^b and the blue peak has a slightly larger velocity shift with respect to the DLA redshift compared to the red peak (see columns 7 and 8 in Table 4). Table 4 also gives the deconvolved FWHM of the red peak obtained through Gaussian fitting (column 9). In section 5.1 we use these values to compare DLAs with high redshift LBGs and Ly α emitters (LAEs).

It is clear from the bottom three panels in Fig. 6 and top three columns in Table 4 that as we keep adding DLAs along the QSOs with high ($r-i$) colors the measured Ly α luminosity over the DLA core as well as L_λ^b and L_λ^r decrease. In addition the significance of blue as well as red peak decreases. This trend is in line with our expectation that the presence of dust in DLAs will destroy the Ly α photons. Based on this trend, naively we would expect the double hump to disappear when we consider sub-sample of DLAs towards QSOs having ($r-i$) in the upper 50 per cent. While this is the case (see the second panel from top in Fig. 6), we notice that the total integrated Ly α luminosity over the core region is similar to what we find for the lower 50 per cent case. This is mainly because of the detection of non-zero luminosity (detected at $\sim 3.4\sigma$ level) in the red part. Indeed, when we consider only the upper 30 per cent of sightlines based on ($r-i$) colours the Ly α luminosity we measure is close to what we measure for the lower 30 per cent case albeit without a clear detection of the double hump. *While the disappearance of the double hump (or decreasing flux in the blue part) with increasing ($r-i$) is consistent with the effect of dust the lack of systematic change in the integrated Ly α luminosity suggests that there are other effects at play while we change ($r-i$).*

It is to be remembered that when we consider the upper 30 per cent we probably have a mixed population of QSOs i.e., QSOs with bluer intrinsic colour reddened by the dust in the DLAs and QSOs that are intrinsically redder compared to the median QSO spectrum. Even if Ly α is present in all these cases the profile shapes of the two populations are expected to be different that can lead to an incoherent addition and lack of a well defined shape for Ly α emission. In addition, from figure 3, of Krogager et al. (2012) one can see that the high H I column density systems may originate from smaller impact parameter when the metallicities are low. If this is the case with the low ($r-i$) sub-sample then the fiber filling factor will also have a role to play. We also notice a possible correlation between $\Delta(r-i)$ and W_{1526} . As seen in the previous section, systems with high W_{1526} tend to have high Ly α luminosity. Therefore, in the sub-samples based on ($r-i$) it is not necessary that the only quantity that varies is the amount of reddening. Therefore interpretation of these results is not straight forward.

4 ABSORPTION LINES IN THE STACKED SPECTRUM

We also generated sets of median stacked spectra to study absorption lines, as described in section 3, for various sub-samples discussed in the previous section. We detect transitions of the low ionization species (e.g. Fe II, Si II, Zn II,

Cr II, Mg I), high-ionization species (Si IV, C IV) and weak transition lines (Fe II λ 2249,2260) as found earlier in the stacked SDSS spectra by York et al. (2006); Khare et al. (2012) and Noterdaeme et al. (2014). In addition, we clearly detect Fe II λ 1611, Ni II λ 1454 and Ti II λ 1910 absorption which were marginally detected in the stacked spectrum of extreme-DLA systems studied by Noterdaeme et al. (2014). The rest equivalent width (W_r) measured for various metal lines in the stacked spectrum of our entire sample as well as different sub-samples, with a single Gaussian fit, are listed in Table A3. Comparison of profiles of different absorption lines seen between different sub-samples are also shown in Fig. A4. We note that most lines are saturated even if the apparent optical depths of the strong absorption lines are small and appear unsaturated due to insufficient BOSS spectral resolution ($R \sim 2000$) and smoothing resulting from redshift uncertainties when co-adding the spectra (York et al. 2006; Sardane et al. 2015; Noterdaeme et al. 2014).

Next, using different absorption lines of Fe II and Si II, that originate from transitions with a broad range of oscillator strengths detected in our stacked spectra, we compute the column density and the effective Doppler parameter (b_{eff}) by constructing a single cloud curve growth (see left panel of Fig. 7 for the sub-samples based on W_{1526}). It is clear that b_{eff} is a function of W_{1526} . Jenkins (1986) has shown that a single cloud curve of growth (COG) gives nearly correct column density when using the W_r of several lines with the line distribution function not having markedly irregular characteristic, even when different lines have large variation in central optical depth and inter velocity dispersion. While spectral resolution of BOSS spectra will not allow us to measure N and b parameter accurately the purpose of using single cloud curve of growth is to find some tracers of column density and velocity field (i.e., b_{eff}).

In Fig. 8, we show the integrated Ly α luminosity in DLA core region (*lower panel*) and in the red part of the DLA trough (*upper panel*) versus b_{eff} . In this figure, we mainly focus on the four sub-samples defined only based on W_{1526} . The b_{eff} value for various sub-samples are given in Table 5 (column 2). These values are much higher than what one measures in individual components seen in high resolution echelle spectra. While comparing the Δv_{90} and b_{eff} measured from high resolution spectrum Noterdaeme et al. (2014) have obtained an empirical relation of $\Delta v = 2.2 b_{\text{eff}} + 0.02 b_{\text{eff}}^2$ which at larger b_{eff} departs from the linear theoretical relation in the Gaussian regime, $\Delta v = 2.33 b_{\text{eff}}$ (see their figure 7). Therefore, b_{eff} we measure is an indication of overall velocity field and not related to the thermal or micro-turbulent motion.

Interestingly we notice nearly the same b_{eff} (i.e., between 35 and 38 km s $^{-1}$) for the sub-samples divided based on $N(\text{H I})$ and z (not shown in this figure). Remember these sub-samples do not show significant difference in their Ly α luminosities. Also, all of them tend to have less Ly α luminosity compared to the high W_{1526} sub-sample. Note, Noterdaeme et al. (2014) have found a $b_{\text{eff}} = 40$ km s $^{-1}$ for their extremely strong DLAs with similar analysis. An increasing trend of Ly α luminosity with b_{eff} is clearly seen while considering the total luminosity in the DLA core as well as the L_λ^r (see Fig. 8). These trends are consistent with high W_{1526} systems originating from gas with high velocity fields and also tend to show higher Ly α luminosity.

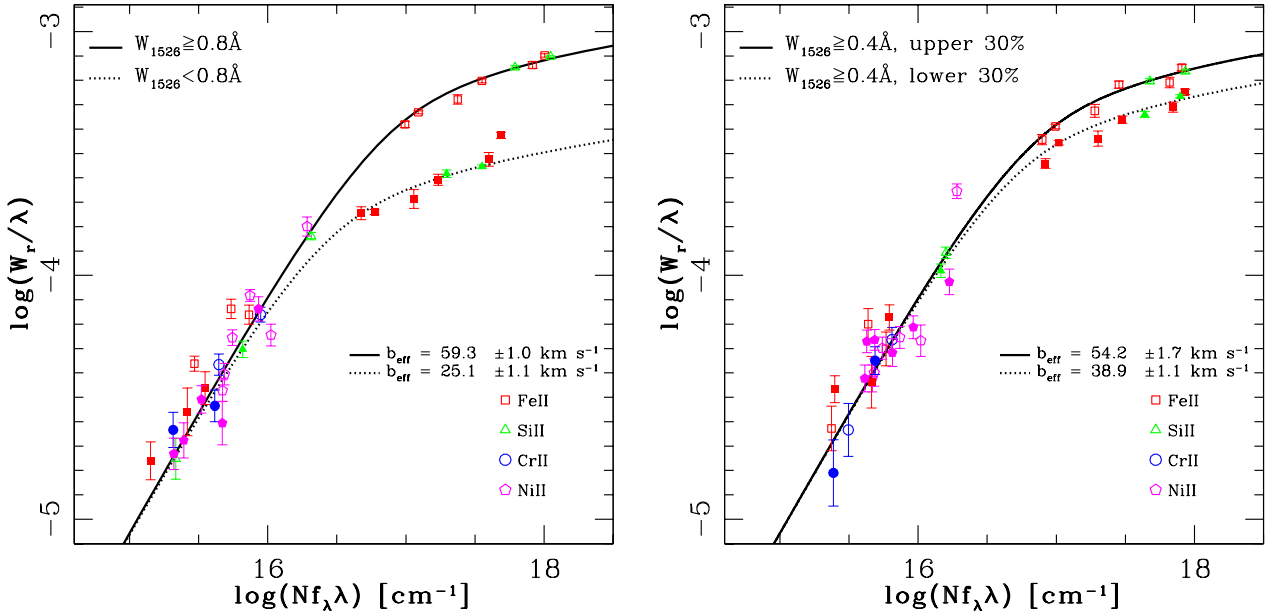


Figure 7. *Left panel:* Single component curve of growth for absorption lines detected in the median stacked spectrum for the sub-samples with $W_{1526} \geq 0.8 \text{ \AA}$ (open squares and solid line) and $< 0.8 \text{ \AA}$ (filled squares and dotted line). The best fitted b_{eff} obtained are also quoted in the figure. *Right panel:* Same for the stacked spectrum of $W_{1526} \geq 0.4 \text{ \AA}$ and considering upper and lower 30% sample from $(r-i)$ color distribution.

Table 5. Parameters estimated using absorption stacks.

sample criteria	b_{eff} (km s $^{-1}$)	Δv_{90} (km s $^{-1}$)	W_{1526} (\AA)	FWHM(C IV) (km s $^{-1}$)	DR^a	FWHM(Si II) (km s $^{-1}$)
$W_{1526} \geq 0.8 \text{ \AA}$	59.3 ± 1.3	201	1.21 ± 0.01	252.8 ± 4.2	1.75	240.1 ± 2.4
$W_{1526} < 0.8 \text{ \AA}$	25.1 ± 0.8	76	0.43 ± 0.01	220.1 ± 6.2	1.63	125.4 ± 2.2
$W_{1526} \geq 0.6 \text{ \AA}$	50.8 ± 1.0	164	1.03 ± 0.01	251.4 ± 4.1	1.72	213.6 ± 2.3
$W_{1526} < 0.6 \text{ \AA}$	21.9 ± 0.6	61	0.37 ± 0.01	197.7 ± 7.5	1.63	114.0 ± 2.6
$W_{1526} \geq 0.4 \text{ \AA}$	45.3 ± 1.0	141	0.85 ± 0.01	250.3 ± 4.0	1.74	192.7 ± 2.2
$N(\text{H I}) \geq 10^{21.23} \text{ cm}^{-2}$	34.4 ± 1.0	100	0.75 ± 0.01	245.0 ± 5.0	1.61	180.0 ± 3.1
$N(\text{H I}) < 10^{21.23} \text{ cm}^{-2}$	36.0 ± 1.3	106	0.61 ± 0.01	237.7 ± 6.4	1.71	167.4 ± 3.6
$z_{\text{abs}} \geq 0.7$	37.2 ± 1.8	110	0.65 ± 0.11	228.3 ± 6.3	1.70	171.3 ± 3.6
$z_{\text{abs}} < 0.7$	37.8 ± 1.0	112	0.69 ± 0.10	246.6 ± 5.1	1.66	175.0 ± 3.1
$(r-i)$ upper 30%	54.2 ± 1.7	179	1.05 ± 0.02	240.5 ± 6.5	1.83	222.4 ± 4.2
$(r-i)$ lower 30%	38.9 ± 1.1	116	0.83 ± 0.01	270.4 ± 7.3	1.68	184.6 ± 3.5

^a C IV doublet ratio, given as $DR = W(\text{C IV}_{1548})/W(\text{C IV}_{1550})$.

Similar dependences are also seen between [O II] luminosity in the stacked spectrum and the equivalent width of Ca II and Mg II absorption lines in the low- z absorbers (Wild et al. 2007; Noterdaeme et al. 2010; Ménard et al. 2011). This could be due to some physical connection between the star formation rate and velocity width (like for example large scale outflows as suggested by Ménard et al. 2011) or an artifact of known correction between the line equivalent width and impact parameter coupled with fiber filling factor decreasing with the impact parameter and hence the rest equivalent width (López & Chen 2012). Both these explanations will work for the Ly α emission also. In addition, we also have the possibility that the Ly α escape fraction being higher at higher W_r (i.e., velocity field). Note that, from the observed W_{1526} and metallicity correlation the Ly α emission will also depend on the metallicity. These

trends are consistent with the suggestion of Möller et al. (2004) based on DLA galaxies detected in their NICMOS sample. However, no such relation is seen with the z and $N(\text{H I})$.

Next we consider two sub-samples based on $(r-i)$ colours of the background QSOs. As discussed in the previous section, the total Ly α luminosity is nearly the same between the sub-samples consisting of the lower and upper 30 per cent sources. This was unexpected based on a simple conjecture that systems towards QSOs with high $(r-i)$ colours and higher dust content should have less Ly α luminosity. The stacked spectra show $b_{\text{eff}} = 39 \text{ km s}^{-1}$ for the lower 30% sub-sample and $b_{\text{eff}} = 54 \text{ km s}^{-1}$ for the upper 30% sub-sample (see right panel in Fig. 7). If one follows the idea of higher the b_{eff} higher will be the intrinsic Ly α luminosity then the higher Ly α luminosity in the upper 30% can

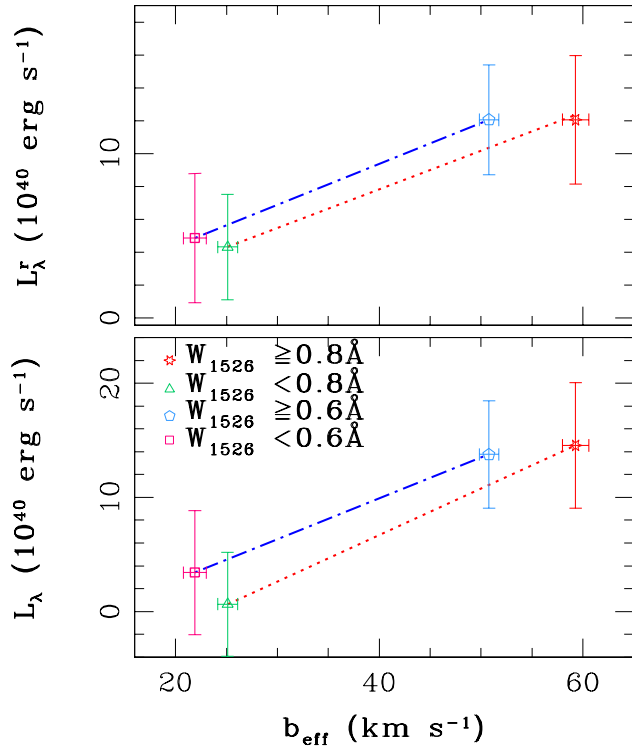


Figure 8. *Lower panel:* The dependence of Ly α luminosity (integrated over the entire DLA core region) on the Doppler parameter (b_{eff}) for the sub-samples with $W_{1526} \geq 0.6, 0.8$ and $< 0.6, 0.8$ Å. *Upper panel:* same for the luminosity seen in the red part of DLA bottom. Note that the significant detection (i.e., $> 3\sigma$ level) is only for three cases with $W_{1526} \geq 0.6$ and 0.8 Å.

be understood as the consequence of systems having more intrinsic Ly α luminosity.

In Table 5 (see column 3), we present the velocity width (Δv_{90}) estimated from the relationship between Δv_{90} and b_{eff} obtained by [Noterdaeme et al. \(2014\)](#), see above). There is a hint of excess Ly α emission with the large values of Δv_{90} . It is clear that the inferred Δv_{90} are more than 100 km s^{-1} in cases where we have significant Ly α detection. Interestingly, we note that in case of direct detection of Ly α emission from DLA host galaxies the Δv_{90} is found to be greater than $\sim 100 \text{ km s}^{-1}$ (see [Fynbo et al. 2010b](#); [Noterdaeme et al. 2012a](#); [Hartoog et al. 2015](#); [Srianand et al. 2016](#)). In a cosmological hydrodynamic simulations, [Bird et al. \(2015\)](#) have shown that the velocity width closely tracks the virial velocity of the DLA host halo, and thus provides an analogue to the halo mass. In their models $\Delta v_{90} \sim 100 \text{ km s}^{-1}$ will corresponds to typically halo mass of $10^{10} - 10^{11} M_{\odot}$. In such halos higher gas accretion rate could lead to high SFR, hence higher intrinsic Ly α and UV emission, albeit with a very small Ly α escape fraction ([Garel et al. 2015](#)). Alternatively the observed low Ly α luminosity be related to the diffuse Ly α emission from the extended region of high mass galaxies. As we noted above the average luminosity is much less (i.e., 2 to 2.5 per cent) than that of an L_{\star} galaxy. We discuss these possibilities in the following section.

We now investigate the dependence of Ly α emission on the high ionization C IV line which probes a wider re-

gion of velocity space than the neutral lines ([Ledoux et al. 1998](#); [Wolfe & Prochaska 2000](#); [Fox et al. 2007](#)). [Fox et al. \(2007\)](#) have shown that high velocity C IV clouds are unbound to the central potential well and traces the outflows. In Fig 9, we plot the Ly α luminosity, integrated over the entire DLA bottom, as a function of C IV equivalent width, FWHM and the C IV doublet ratio (i.e., $DR = W(\text{C IV}_{1548})/W(\text{C IV}_{1550})$) for the sub-samples based on W_{1526} . The measured line widths (FWHM), corrected for instrumental resolution, DR and width of the Si II line are also summarized in Table 5. As noted by [Fox et al. \(2007\)](#) C IV lines are wider than Si II lines. A trend of increasing Ly α luminosity with increasing W_{τ} and FWHM of C IV is clearly noticeable. In addition, the larger doublet ratio (i.e., optically thin gas) and higher equivalent width suggest that the winds from the galaxy are responsible for the absorption ([Bouché et al. 2006](#); [Christensen et al. 2009](#)). From Table 5, it is clear that there is very little difference in C IV (FWHM) between the sub-samples defined based on $(r - i)$ colours. The correlation between L_{λ} and b_{eff} is not present when we consider the two sub-samples based on $(r - i)$ colours as discussed before. This once again reiterates the importance of dust and difficulties related to interpreting Ly α profile in the stacked spectrum.

In summary, the Ly α emission from DLAs may be originating from systems with large velocity widths in both high and low ions. There are also indications that the metallicity and dust may have important role to play in deciding the total Ly α luminosity and the profile shape.

5 DISCUSSION

In this section, we discuss implications of our Ly α measurements for different stacked spectra and draw some broad conclusions on the nature of high- z DLAs.

5.1 Ly α emission line profile

The Ly α emission line profile is a powerful probe of the star formation and associated feedback processes (i.e., infall and/or outflows) in young galaxies. In an extremely opaque static medium Ly α escape through successive resonance scattering leading to a double-humped profile, with the position of the peaks determined by column density, temperature, and kinematics of the medium ([Neufeld 1990, 1991](#); [Verhamme et al. 2006](#); [Hansen & Oh 2006](#); [Dijkstra et al. 2006](#); [Dijkstra 2014](#)). In addition, presence of bulk motions (e.g., outflow/inflow) and scattering by dust in the H I gas can further modify the emergent Ly α profile. For instance, the scattering through an outflowing (respectively inflowing) medium results in an overall redshift (respectively blueshift) of the Ly α spectral line with enhanced red (respectively blue) peak and suppressed blue (respectively red) peak ([Dijkstra et al. 2006](#); [Barnes & Haehnelt 2010](#)).

We detect Ly α emission predominantly in the red part of the Ly α trough. This implies the presence of outflows in high- z DLAs. We detect flux in the red part at 2.8σ when we consider the full sample and with more than 3σ level when we consider the sub-samples with $W_{1526} \geq 0.4$ Å, 0.6 Å and 0.8 Å (see Table 2 and Table A1). In these cases, the average Ly α luminosity is found to be consistent within

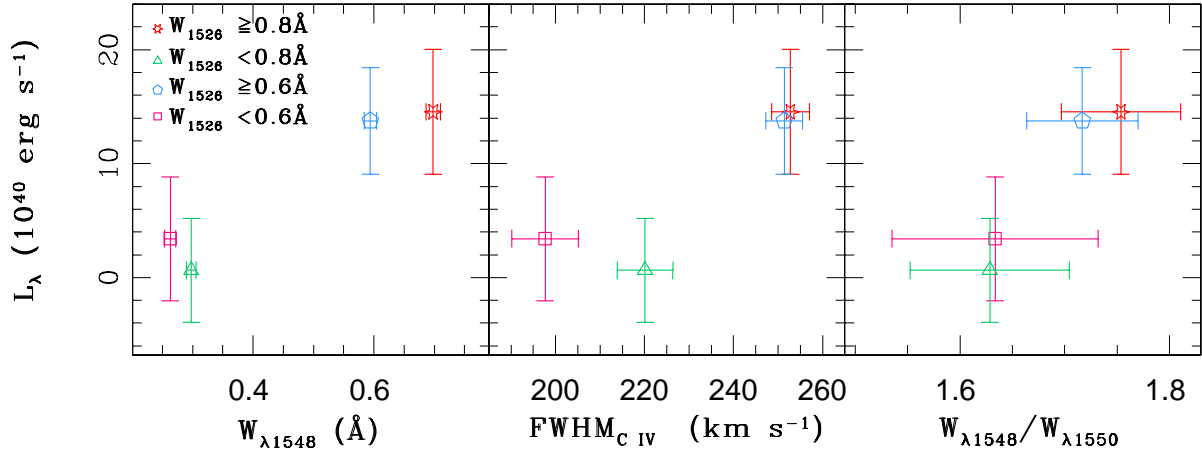


Figure 9. The dependence of Ly α luminosity (integrated over the entire DLA core region) on the equivalent width, FWHM of C IV absorption and the doublet ratio (i.e., W_{1548}/W_{1550}) for the sub-samples with $W_{1526} \geq 0.6, 0.8$ and $< 0.6, 0.8$ Å.

Table 6. The star formation rate and surface brightness corresponding to the Ly α luminosity seen in the red and blue part of DLA profile (median stack) in bootstrap analysis.

Sample	SFR ($M_{\odot} \text{yr}^{-1}$) ^a			surface brightness ^b ($\times 10^{-19} \text{ erg s}^{-1} \text{ cm}^{-2} \text{ arcsec}^{-2}$)
	DLA-bottom	blue-part	red-part	
Full with 90% bootstrap	≤ 0.55	≤ 0.39	≤ 0.39	≤ 3.93
Full with 80% bootstrap	≤ 0.58	≤ 0.41	≤ 0.42	≤ 4.17
$W_{1526} \geq 0.4 \text{ Å}$	0.71 ± 0.21	≤ 0.45	0.65 ± 0.13	6.66 ± 1.56
$W_{1526} \geq 0.8 \text{ Å}$	≤ 0.87	≤ 0.61	0.64 ± 0.17	6.51 ± 2.11
$W_{1526} < 0.8 \text{ Å}$	≤ 0.85	≤ 0.58	≤ 0.61	≤ 6.58
$N(\text{H I}) \geq 10^{21.23} \text{ cm}^{-2}$	≤ 0.78	≤ 0.55	≤ 0.56	≤ 5.51
$10^{21} \leq N(\text{H I}) < 10^{21.23} \text{ cm}^{-2}$	≤ 0.76	≤ 0.53	≤ 0.55	≤ 5.53
$z_{\text{abs}} \geq 2.7$	≤ 0.84	≤ 0.58	≤ 0.60	≤ 4.79
$z_{\text{abs}} < 2.7$	≤ 0.73	≤ 0.51	≤ 0.52	≤ 6.43
$(r-i) \geq 0.1$	≤ 0.79	≤ 0.56	≤ 0.55	≤ 4.98
$(r-i) < 0.1$	≤ 0.78	≤ 0.53	≤ 0.57	≤ 5.26

^a a 3σ upper limit is given in case of non-detection. Here, the errors are purely statistical and depends on the value of assumed f_{esc} and IMF. See Section 5.3 for details of assumption involved in this estimate.

^b Surface brightness corresponding to the Ly α luminosity seen in the red part of DLA bottom.

the $\sim 3\sigma$ upper limit of $\sim 21.8 \times 10^{40} \text{ erg s}^{-1}$ obtained by coadding 341 low column density ($\log N(\text{H I}) \geq 20.62$) DLAs by Rahmani et al. (2010). However, less than the Ly α luminosity of $(60.0 \pm 20.0) \times 10^{40} \text{ erg s}^{-1}$, seen in the composite spectrum of extremely strong DLAs ($\log N(\text{H I}) \geq 21.7$) by Noterdaeme et al. (2014). We find the Ly α luminosity being higher for systems with higher W_{1526} which indicates that high metallicity DLAs could be associated with high star forming galaxies. Recently, the detection rate of DLA host galaxies is found to be higher towards high-metallicity DLAs (Fynbo et al. 2010b, 2011, 2013; Krogager et al. 2012, 2013). These galaxies show either no Ly α emission or a suppressed blue peak.

For the sub-samples with $W_{1526} \geq 0.4 \text{ Å}$, 0.6 Å and 0.8 Å with clear Ly α detection, we model the red peak with a Gaussian profile and measure the centroid shift with respect to the redshift defined by the absorption lines detected in the quasar spectrum. As evident from Fig. 4 the final profile shape of the Ly α emission in the stacked spectrum

depends on the statistics used. When we use median combined spectrum, we measure $\Delta v_{Ly\alpha}^r = 385 \pm 28$, 331 ± 28 and $337 \pm 32 \text{ km s}^{-1}$ for the sub-samples with $W_{1526} \geq 0.4 \text{ Å}$, 0.6 Å and 0.8 Å respectively. When we use the weighted mean spectrum, we get $\Delta v_{Ly\alpha}^r = 321 \pm 32$, 395 ± 34 and $295 \pm 56 \text{ km s}^{-1}$ for the three cases. From Table 2, we can see the mean $N(\text{H I})$ in all these cases are nearly the same i.e., $\log N(\text{H I}) \sim 21.25$. In a pure static medium, we expect $\Delta v_{Ly\alpha}^r$ in the range 613–417 km s^{-1} if we assume H I gas temperature to be in the range, 10^3 to 10^4 K (Dijkstra 2014, see their eq. 21).

Interestingly, the Ly α emission line profiles associated with a handful of confirmed DLA host galaxies are found to be predominantly redshifted with typical velocity offsets ranging from 10 – 400 km s^{-1} (Møller & Warren 1993; Møller et al. 2002; Möller et al. 2004; Fynbo et al. 2010b; Krogager et al. 2012; Hartoog et al. 2015; Srianand et al. 2016). Thus, what we measure in the stacked spectra are consistent with these individual measurements. In addition,

Noterdaeme et al. (2014) have shown that the Ly α emission in the composite spectrum of extremely strong DLAs also show a redshifted profile relative to the systemic redshift. Till now only one DLA with Ly α emission ($z_{\text{abs}} = 2.207$ towards the quasar SDSS J113520.39–001053.56) shows a classical double hump profile (Noterdaeme et al. 2012a; Kulkarni et al. 2012). Even in this case detailed modelling of the Ly α radiative transport favors the emission being scattered from an outflowing gas (Noterdaeme et al. 2012a).

In the case of high- z LBGs and LAEs whenever systematic redshifts can be determined using optical nebular emission lines the Ly α emission line profile is found to be asymmetric with the peak emission being redshifted in the majority of the cases. The typical peak shift measured is $\sim 200 \text{ km s}^{-1}$ in the case of LAEs (Shibuya et al. 2014; Erb et al. 2014; Song et al. 2014; Trainor et al. 2015) and $\sim 400 - 600 \text{ km s}^{-1}$ in the case of LBGs (see Steidel et al. 2003, 2010; Kulas et al. 2012). It has also been suggested that the shifts seen in the case of LAEs and LBGs are statistically different. This could be attributed either to the differences in $N(\text{H I})$ or to the H I covering factor. Taken it at face value the $\Delta v_{\text{Ly}\alpha}$ we measure for DLAs is higher than the mean value typically seen in the case of LAEs but less than that of LBGs.

As discussed in the Section 3.6, a clear double hump profile is detected when we use DLAs detected towards bluer quasars. The two peaks are separated $\sim 650 \text{ km s}^{-1}$, $L_{\lambda}^{\text{r}}/L_{\lambda}^{\text{b}} \sim 2$ and red part has an FWHM of $\sim 200 \text{ km s}^{-1}$. About 30% of LBGs (Kulas et al. 2012) and 50% of LAEs (Yamada et al. 2012; Hashimoto et al. 2015) show multiple peaks in their Ly α emission with a typical peak separations of $\sim 500 \text{ km s}^{-1}$ and 800 km s^{-1} respectively, for LAEs and LBGs (Kulas et al. 2012; Hashimoto et al. 2015; Trainor et al. 2015). In addition, the mean FWHM of the red peak of Ly α line in LAEs and LBGs are found to be ~ 260 and 364 km s^{-1} , respectively (Trainor et al. 2015). The average property we measure for the sub-samples with double hump Ly α profile are intermediate between LAEs and LBGs. However, it is interesting to understand the connection between the appearance of a double hump feature and low reddening of the quasars. A double hump feature is naturally produced when Ly α transport occur with nearly static H I gas with very little dust and weak bulk motions. Another possible explanation is that systems towards blue quasars having large velocity infall. However, a clear answer to our finding can only come from a detailed analysis of individual systems with double hump detections in front of blue quasars.

Some caution has to be exercised while comparing the DLA measurements with those of LBGs and LAEs. Noterdaeme et al. (2010) have detected nebular emission lines from $z \sim 0.6$ Mg II systems in the SDSS fiber spectra of distant QSOs. From their figure 7, we can see that the relative velocity between the absorption redshift and the redshift from the nebular line can be between $\pm 100 \text{ km s}^{-1}$. If similar shifts exist between the line-of-sight where we detect the DLA absorption and the star forming regions from where the Ly α emission originates then the intrinsic Ly α emission profile will be smeared by this additional random velocities. *While this effect prevents us from establishing a link between DLAs and either of LAEs or LBGs, the analysis presented*

here suggests that the average Ly α profile we find follows the trends seen in the case of LBGs and LAEs.

5.2 Fluorescent Ly α emission induced by UV background

We now explore the Ly α emission being induced by meta-galactic UV background impinging on the optically thick gas as a possible mechanism for the Ly α emission from DLAs. For this, we use the recent computation of the background ionizing radiation by Khaire & Srianand (2015a,b), accounting for the contributions from both quasars and galaxies (with typical escape fraction, f_{esc} , of 2 and 4 per cent for galaxies). For the f_{esc} of 0, 2 and 4 per cent, the integrated unidirectional flux of the H I ionizing photons (i.e., $\phi_0 = \int_{\nu_0}^{\infty} \pi I_{\nu} d\nu / h\nu$) at $z \sim 2.7$ are found to be $\sim 9.1 \times 10^4$, 1.3×10^5 and $1.7 \times 10^5 \text{ photons s}^{-1} \text{ cm}^{-2}$, respectively (see Shull et al. 2014). If we assume an arcsec² optically thick H I gas cloud in photoionization equilibrium with this background, it will produce a surface brightness of $\sim 3.1 \times 10^{-20}$, 4.6×10^{-20} and $6.2 \times 10^{-20} \text{ erg s}^{-1} \text{ cm}^{-2} \text{ arcsec}^{-2}$. These values will be reduced if the clouds are observed at some inclination angle.

Note that, in the presence of a local ionizing source the observed surface brightness will increase and is related to surface brightness induced by UV background as, $\text{SB} = (1 + b)\text{SB}_{\text{bgr}}$. Here b is the boost factor defined as the ratio of H I photoionization rate (Γ_{HI}) from the local source to that of the UV background. Table 6 lists surface brightness corresponding to the Ly α luminosity measured in the red part or 3σ upper limits. It is clear that, in cases where luminosity is measured at $> 3\sigma$ level, the measured Ly α surface brightness requires a boost by a factor of more than 6 even if we consider meta galactic UV-background computed with 4 per cent escape fraction for UV photons from galaxies. In particular, for systems with $W_{1526} \geq 0.8 \text{ \AA}$ we need a boost in the Ly α continuum flux by at least a factor ~ 10 from local sources of excitation probably from *in-situ* star formation or from star forming regions close to the DLAs. In what follows, we discuss the implication of a local radiation field in some detail.

5.3 In-situ star formation

Assuming that the Ly α photons mainly originate from H II regions around massive stars embedded in the DLAs and case B-recombination (Osterbrock & Ferland 2006), we relate the Ly α luminosity to the star formation rate SFR (\dot{M}_{SF}) as:

$$L_{\text{Ly}\alpha} = 0.68 h\nu_{\alpha} (1 - f_{\text{esc}}) N_{\gamma} \dot{M}_{\text{SF}}. \quad (1)$$

Here, $h\nu_{\alpha} = 10.2 \text{ eV}$, is the energy of the Ly α photons. At the redshift of interest in this work $f_{\text{esc}} \leq 0.04$ based on the Γ_{HI} measurement using Ly α absorption by the intergalactic medium (Khaire et al. 2016). Vasei et al. (2016) have found a $f_{\text{esc}} \leq 0.08$ using deep HST imaging of a gravitationally lensed galaxy at $z \sim 2.38$. In our calculations we use $f_{\text{esc}} = 0.04$. The N_{γ} represents the number of ionizing photons released per baryons of star formation. We use $N_{\gamma} = 9870$, corresponding to the average metallicity, i.e. $Z/Z_{\odot} = -1.5$, of high redshift DLA absorbers and a Salpeter

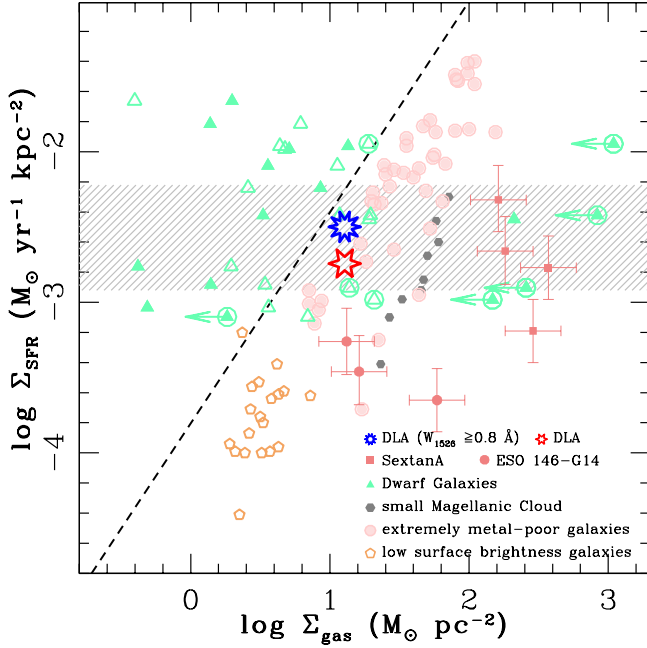


Figure 10. The comparison of surface density of star formation and total (solid symbols) and HI (open symbols) gas surface density in DLAs with different classes of star forming galaxies. Orange points (*open pentagon*) represent low surface brightness galaxies (Wyder et al. 2009), black points (*small hexagon*) spatially resolved observations of Small Magellanic Cloud (Bolatto et al. 2011), purple points (*circle*) extremely metal poor galaxies (Filho et al. 2016), green points (*triangle*) dwarf galaxies (Cormier et al. 2014), brown points (*square*) resolved observations of extremely metal poor galaxies SextanA and (*circle*) ESO 146-G14 (Shi et al. 2014). The dashed line corresponds to Kennicutt-Schmidt law (Kennicutt & Evans 2012). The hatched region shows the surface brightness seen in the outskirts (i.e., 3 – 6 kpc) of LBGs (Rafelski et al. 2011).

initial mass function with $\alpha = 2.35$, given in Rahmani et al. (2010, references therein). Note that the observed Ly α luminosity depends on the escape fraction ($f_{esc}^{Ly\alpha}$) of Ly α photons and related to the emitted Ly α luminosity ($L_{Ly\alpha}$) as $L_{Ly\alpha}^{obs} = f_{esc}^{Ly\alpha} L_{Ly\alpha}$. We use the $f_{esc}^{Ly\alpha}$ to be 5 per cent, as is estimated for the high-redshift ($z \sim 2.2$) star forming galaxies by Hayes et al. (2010). Based on the Ly α to the H α luminosity ratio Trainor et al. (2015) have recently estimated the $f_{esc}^{Ly\alpha}$ to be 30 per cent for the LAE. For our purpose, we use 5% escape in our analysis.

The SFR corresponding to the Ly α luminosity in the entire DLA bottom as well as in the red and blue part for various sub-samples, measured in our bootstrap analysis, are given in Table 6. Note, if $f_{esc}^{Ly\alpha}$ is 30 per cent, as seen in the case of LAEs, then the inferred SFR will be less than what is given in Table 6 by a factor 6. The average SFR in the stacked spectrum of our full sample is found to be $\leq 0.4 \text{ M}_{\odot} \text{ yr}^{-1}$ in the red and blue part and also in the entire DLA trough. However, the sub-samples with $W_{1526} \geq 0.4 \text{ \AA}$ and $W_{1526} \geq 0.8 \text{ \AA}$ show a slightly higher SFR at $\sim 0.7 \text{ M}_{\odot} \text{ yr}^{-1}$ for the total and the red part. In addition,

for the sub-samples based on $N(\text{H I})$ and z_{abs} the 3σ upper limit on SFR is found to be $\sim 0.6 \text{ M}_{\odot} \text{ yr}^{-1}$ (see also Table 6).

Next, we explore the Kennicutt-Schmidt (KS) relation between the gas surface mass density and the star formation rate per unit surface area in DLA galaxies. Assuming the typical size of the DLA galaxies to be $R = 8 \text{ kpc}$ (the fiber filling factor of 1) we compute the average SFR per unit area to be $\log \Sigma_{SFR} = -2.7$ and $-2.5 \text{ M}_{\odot} \text{ yr}^{-1} \text{ kpc}^{-2}$ in the red part of DLA bottom for our entire sample and the sub-sample with $W_{1526} \geq 0.8 \text{ \AA}$, respectively. As the fiber filling factor may be smaller than one, the measured Σ_{SFR} values should be a lower limits. For the mean $\log N(\text{H I}) = 21.23$, probed in this work, the expected average SFR is about $0.01 \text{ M}_{\odot} \text{ yr}^{-1} \text{ kpc}^{-2}$, if one considers the KS relation for low redshift star forming galaxies (Kennicutt 1998a,b). The surface SFR densities in DLA galaxies are a factor of ~ 6 lower than what one would predict from the local star formation law (see also, Chelouche & Bowen 2010; Rahmani et al. 2010; Rafelski et al. 2011).

In Fig. 10, we compare the gas surface density (Σ_{gas}) with the surface SFR (Σ_{SFR}) in different kinds of galaxies with what we measure for DLAs. It is clear from the figure that the DLAs occupy the region that is generally populated by low metallicity dwarf galaxies and extremely metal poor (i.e. $Z < 0.1Z_{\odot}$) galaxies (Wyder et al. 2009; Bolatto et al. 2011; Shi et al. 2014; Cormier et al. 2014; Filho et al. 2016). In this figure we also compare the surface brightness seen in the outer region of LBGs in the stacked images by Rafelski et al. (2011). Our measurements and the limits are consistent with this range. It is interesting to note that in the case of DLAs despite $\log N(\text{H I}) \geq 21$ we do not detect H_2 molecules in our stacked spectrum (see Noterdaeme et al. 2015, for $\text{H}_2\text{-H I}$ transition in DLAs using individual H_2 measurements) so the surface mass density is mainly atomic. However, even in the case of dwarf galaxies a considerable contribution to the measured surface mass density comes from molecular gas. While H I emission is widespread in the dwarf galaxies, regions with $\log N(\text{H I}) \geq 21$ project smaller cross-section and usually localized to the star forming regions even if there is no one to one correspondence between SFR and $N(\text{H I})$ (Begum et al. 2006; Roychowdhury et al. 2014). Therefore, in this scenario the continuum and Ly α emission associated with the H I gas can be well within the SDSS fiber.

The low star formation efficiency in low metallicity dwarf galaxies and extremely metal poor galaxies is mainly attributed to the (i) low cooling rate in metal poor environments (Filho et al. 2013, 2016); (ii) galactic winds which can suppress the SFR by throwing more than 80% of gas back to the circum-galactic medium (Sánchez Almeida et al. 2014) and/or (iii) related to the star formation in compact regions which are fed by the accretion of metal poor H I gas by cold cosmological accretion (Ekta & Chengalur 2010; Sánchez Almeida et al. 2014). The same may be the reason for low SFR seen in DLA galaxies as well, as the DLAs are also found to have a low average metallicity, i.e., $\sim 1/10\text{th}$ of solar, at $z \sim 2$ (Rafelski et al. 2012; Noterdaeme et al. 2014) and signatures of outflows as an off-centered Ly α emission in our stack.

The low surface brightness galaxies or the low surface brightness outer regions of luminous galaxies contributing to the high- z DLA population is a good possibility, even

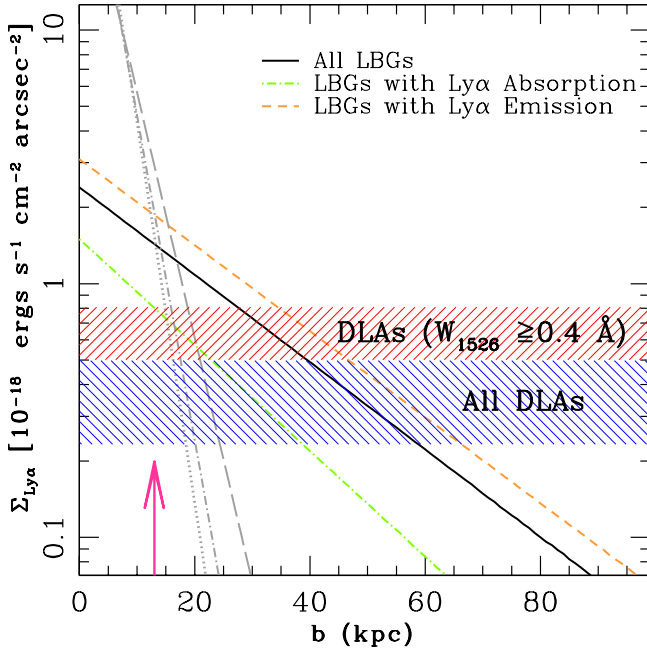


Figure 11. The average surface brightness profile of the $\text{Ly}\alpha$ emission in a stacked images of 92 LBGs (solid black) and in a sub-sample with LBGs seen in $\text{Ly}\alpha$ emission (orange dashed) and in $\text{Ly}\alpha$ absorption (green dot-dashed) by Steidel et al. (2011). The gray lines represent the average surface brightness profile of continuum light (at 1220 Å) for all LBGs (dashed dotted) as well as the sub-samples with only $\text{Ly}\alpha$ emission (dotted) and absorption (dashed). The hatched region show the surface brightness seen in our DLA stacks for entire sample (blue) and for a sub-sample (red) with $W_{1526} \geq 0.4$ Å, respectively. The arrow represent the expected R_* for unit covering factor of H I gas around galaxies from discussion in Section 5.4.

though at low- z such galaxies do not contribute appreciably to the high $N(\text{H I})$ absorbers studied here (Patra et al. 2013). While we expect the number density of low mass galaxies to be much higher at higher z , $\text{Ly}\alpha$ forest - DLA cross-correlation analysis suggests that most of the high- z DLAs may originate from a biased regions with halos of $10^{12} M_\odot$ (Font-Ribera et al. 2012).

Next, we consider the possibility of DLAs originating from passive H I gas at the external regions of massive star forming galaxies. In this scenario, the $\text{Ly}\alpha$ emission will be detected either when the galaxy light falls inside the fiber (i.e., impact parameter less than 8 kpc) or when the Lyman continuum photons from the host galaxy inducing the $\text{Ly}\alpha$ fluorescence emission from the extended gas (i.e., the so called $\text{Ly}\alpha$ halo).

5.4 Star forming galaxies at small impact parameter

The number of DLAs at $z \sim 2.7$ having $\log N(\text{H I}) \geq 21.0$ per unit absorption distance is estimated to be $dN/d\mathcal{X} \approx 0.028$, by integrating over the column density distribution function $f_{\text{HI}}(N, \mathcal{X})$ from Noterdaeme et al. (2009). This can be used to derive the co-moving incidence of star forming galaxies

at high redshift (LBGs) as:

$$dN_{\text{LBGs}}(L > L_{\min})/d\mathcal{X} = (1+z)^2 f \int_{L_{\min}}^{\infty} \pi R(L)^2 \phi(L) dL. \quad (2)$$

Here, $R(L)$ represents size (or impact factor) of the H I gas below which the required $N(\text{H I})$ will be produced in a galaxy with luminosity L . We use a power-law relation, i.e., $R(L) \propto L^{0.4}$, obtained from H I size-optical luminosity relation from field galaxies in ALFALFA survey which is determined based on the galaxy R-band luminosity (Toribio et al. 2011). The f factor is the gas filling factor which is considered to be one. We use the UV luminosity function of LBGs by Reddy & Steidel (2009) at redshifts $1.9 \leq z \leq 2.7$, with best fit Schechter function parameter of $\phi^* = 2.75 \times 10^{-3} \text{Mpc}^{-3}$, $M_{\text{AB}}^*(1700\text{\AA}) = -20.70$ and $\alpha = -1.73$. Using the above scaling relation, $R(L) = R_*(L/L_*)^{0.4}$, the equation (2) becomes:

$$\frac{dN_{\text{LBGs}}}{d\mathcal{X}} = \pi R_*^2 (1+z)^2 f \int_{L_{\min}}^{\infty} \left(\frac{\phi^*}{L_*}\right) \left(\frac{L}{L_*}\right)^{(\alpha+0.8)} \exp\left(-\frac{L}{L_*}\right) dL \quad (3)$$

Owing to the large magnifications by a lensing cluster Alavi et al. (2014) have probe the LBGs down to very faint magnitudes, $M_{1500} < -13$ mag, about 100 times fainter than previous studies at the same redshift (Reddy & Steidel 2009). They have shown that the UV luminosity function of LBGs shows no turnover up to $M_{1500} < -13$ mag and have a faint end slope, $\alpha = 1.74$, similar to Reddy & Steidel (2009). We compute the impact factor, $R \sim 13$ kpc, below which required $N(\text{H I})$ will be produced by an L^* galaxy by integrating the above equation down to $L_{\min} = 0.001 L^*$. It implies a high probability for the L^* galaxy to lie outside the small region of 8 kpc probed by the BOSS fiber. Alternatively, taking the maximum value of R to be ~ 8 kpc (corresponding to the fiber size) in above scaling relation $R = R_*(L/L_*)^\alpha$, we find the maximum luminosity of a galaxy which will come inside the fiber to be $0.3 L^*$. In other words, the majority of galaxies contributing directly to the average luminosity seen in stacked spectrum will be below $\sim 0.3 L^*$.

The average luminosity of LBGs with luminosity ranging from $0.001 - 0.3 L^*$ is given as:

$$\langle L_{\text{LBG}} \rangle = \frac{\int_{L_{\min}}^{L_{\max}} L \phi(L) dL}{\int_{L_{\min}}^{\infty} \phi(L) dL}. \quad (4)$$

We find the average UV luminosity of LBGs to be $1.34 \times 10^{42} \text{erg s}^{-1}$, corresponds to a SFR of $0.12 M_\odot \text{yr}^{-1}$. Interestingly, this is comparable to the average SFR of $0.09 < \text{SFR} < 0.27 M_\odot \text{yr}^{-1}$ (2σ limit) seen in direct imaging of DLA host galaxies within 2 and 12 kpc aperture sizes by Fumagalli et al. (2015), albeit for DLAs with lower $N(\text{H I})$ than what we consider here. Note that if we assume the gas filling factor to be less than 1, then R_* will be > 13 kpc and $L_{\max} < 0.3 L_*$ and the average UV luminosity will be even lower than the above quoted value. The expected SFR within 12 kpc aperture, using the above formalism, is found to be $0.14 M_\odot \text{yr}^{-1}$. Therefore, allowing for the impact parameter for a given $N(\text{H I})$ to scale with optical luminosity (as seen in the local universe) for high- z DLAs gives the mean SFR in the correct ballpark value. Converting the average UV luminosity estimates into $\text{Ly}\alpha$ luminosity is not straight forward as the fraction of $\text{Ly}\alpha$ emitting galaxies may be a function of optical luminosity. However, one can

get a simple estimate by substituting our constraint on SFR in eq 1. If we use $f_{esc} = 0.04$ then in order to explain the Ly α luminosity we find for high W_{1526} sub-samples we need $f_{esc}^{Ly\alpha} = 0.22$. This is in between the values found for LBGs (i.e., 5 per cent) and LAEs (i.e., 30 per cent).

In the above discussion, we found most of the Ly α emission from bright galaxies associated with a DLA will be outside the SDSS fiber. However, even in this case Ly α fluorescence from the large extended regions can still contribute to the Ly α emission inside the fiber. Extended diffuse Ly α emitting regions (up to 80 kpc radius) are detected around high redshift LAEs and LBGs in recent observations by stacking analysis (Hayashino et al. 2004; Steidel et al. 2011; Matsuda et al. 2012; Feldmeier et al. 2013; Momose et al. 2014). The presence of these diffuse Ly α emitting halos (LAHs) are also predicted by numerical simulations (Laursen & Sommer-Larsen 2007; Zheng et al. 2011; Dijkstra & Kramer 2012; Verhamme et al. 2012; Jeesson-Daniel et al. 2012).

Momose et al. (2016) have found prominent LAHs around LAEs with faint Ly α luminosities, bright UV luminosities, and small Ly α equivalent width. The extent of the LAHs is found to be dependent on the environment, where LAHs in low-density environment are found to be smaller than the higher density environments having a typical scale length of ~ 9.1 and 20.4 kpc, respectively (Matsuda et al. 2012; Momose et al. 2014). In addition, in continuum-subtracted Ly α emission images of LBGs Steidel et al. (2011) have found similar diffuse Ly α halos for all the galaxies, irrespective of whether the Ly α is seen in emission or absorption, up to radii of ~ 80 kpc. In Fig. 11, we compare the average Ly α surface brightness profile found by Steidel et al. (2011) around the LBGs with our measurements. Our discussions in the previous section suggests an L_* galaxy will have a typical impact parameter of ~ 13 kpc. It is clear from the figure that surface brightness contributions at these impact parameters will be much higher than the average we find for our samples. Inclusion of this contribution will increase the Ly α luminosity inside the fiber from stars that do not contribute to the continuum stacked image. Therefore, the $f_{esc}^{Ly\alpha}$ can be smaller than 0.22 we infer to match our Ly α luminosities with the SFR constrains from the stacking experiment.

6 SUMMARY

In order to probe the star formation in neutral gas clouds at high redshift, we perform a stacking analysis of 704 DLAs with a large H I column density ($\log N(\text{H I}) \geq 21$) and a median redshift of ~ 2.7 . We generate both emission and absorption line stacked spectrum for various sub-samples based on $N(\text{H I})$, z_{abs} , W_{1526} and $(r-i)$ colours of QSOs which led us to the following conclusions :

(1) For the full sample, we measure the Ly α luminosity of $(5.2 \pm 3.3) \times 10^{40} \text{ erg s}^{-1}$ when we integrate the luminosity over the full core regions of the DLA in the median spectrum. Similar values are obtained when we considered the stacked spectra obtained using weighted mean and 3σ clipped weighted mean. This luminosity is ≤ 0.1 per cent of the Ly α luminosity of L_* galaxies at these redshifts. In the bootstrap analysis, the measured luminosities in the red

and blue part of the core regions of the DLA troughs in the median stacked spectrum are $(-1.1 \pm 2.4) \times 10^{40} \text{ erg s}^{-1}$ and $(6.9 \pm 2.5) \times 10^{40} \text{ erg s}^{-1}$ respectively, with a $\sim 2.8 \sigma$ excess Ly α emission in the red part of the DLA trough.

(2) In the sub-samples based on W_{1526} we find the Ly α luminosities of $(13.5 \pm 4.1) \times 10^{40} \text{ erg s}^{-1}$ and $(14.6 \pm 5.5) \times 10^{40} \text{ erg s}^{-1}$ when we integrate the luminosity over the core of Ly α trough in the median spectrum for $W_{1526} \geq 0.4$ and 0.8 \AA respectively. These luminosities are mainly contributed from the red part with respective luminosities of $L_{\lambda}^r = (12.3 \pm 2.9) \times 10^{40} \text{ erg s}^{-1}$ and $(12.1 \pm 3.9) \times 10^{40} \text{ erg s}^{-1}$. Blue parts have luminosities consistent with zero. For systems with Si II detections having $W_{1526} < 0.8 \text{ \AA}$ we find the Ly α luminosity to be $(0.6 \pm 4.5) \times 10^{40} \text{ erg s}^{-1}$. Even in this case most of the observed luminosity comes from the red part albeit with a significance of 1.3σ level. As the median $N(\text{H I})$ in all these sub-samples are the same, the difference in the Ly α luminosity are not likely related to the differences in the H I optical depth. Prochaska et al. (2008) have found a strong correlation between W_{1526} and metallicity using echelle spectroscopic data. This correlation has been interpreted as a mass-metallicity relation as high W_{1526} absorption tend to trace low optical depth clouds in the halo or outflowing gas. Thus the enhanced Ly α luminosity in the high W_{1526} could be an indication of high star formation in high metallicity systems together with easier escape of Ly α photos enabled by the large outflowing gas. We measure large b_{eff} for systems with high W_{1526} which supports this hypothesis.

(3) The sub-samples based on $N(\text{H I})$ do not show any detectable difference in the measured Ly α luminosities either in the full core region or in the red part alone. The same is the case when we divided the sample into two redshift bins. We note that all the four sub-sample have nearly similar mean W_{1526} (see Table A3).

(4) The sub-samples based of $(r-i)$ colours and $W_{1526} > 0.4 \text{ \AA}$ show a double hump profile for the low $(r-i)$ sub-sample. The double hump disappears when we add more and more red QSOs sightlines to this sample. However, total Ly α luminosity does not show any monotonous trend with $(r-i)$. In addition, the $L_{\lambda}^r/L_{\lambda}^b$, FWHM and peak separation are intermediate between what is seen in LBGs and LAEs. However to uniquely identify the reason behind the appearance of double humped Ly α line toward blue QSOs we need detailed analysis of such individual systems using radiative transfer models. Establishing any trend between the dust indicators and Ly α profile will help us to discriminate between different models, such as (i) static medium (Neufeld 1990; Zheng & Miralda-Escudé 2002; Dijkstra et al. 2006), (ii) expanding/inflowing shell (Ahn et al. 2003; Verhamme et al. 2006; Schaerer et al. 2011) or (iii) multiphase media (Gronke & Dijkstra 2016), of the Ly α radiative transport in DLAs. As these models predict different shape as a function of dust content.

(5) In our full sample as well as in all the sub-samples, we detected Ly α emission predominantly in the red part of the Ly α trough albeit with varied significance. The measured shift in the peak location of Ly α emission with respect to the absorption redshift is in the range $300\text{-}400 \text{ km s}^{-1}$. The redshifted profiles are typical of what is seen in the case of LBGs and LAEs at the same redshifts. In these cases the observed redshifted Ly α profiles are considered as a signa-

ture of predominantly outflowing gas in these galaxies. Thus the Ly α profile we measure in the case of high- z DLAs are consistent with the presence of outflowing gas. The measured shift in DLAs are higher than what is typically seen in LAEs but less than those of LBGs. However, as our reference redshift is the absorbing gas along the QSO sightline and not the non-resonant nebular emission from the galaxy itself, we need to exercise caution in interpreting this result.

(6) Using the updated metagalactic UV background radiation contributed by QSOs and galaxies, we find the expected Ly α fluorescence is 4 to 10 times less than what we measure. This means most of the DLAs are not passive clouds in ionization equilibrium with the metagalactic UV background. Local excess ionizing radiation either from a nearby star forming region or from *in-situ* star formation is needed to produce the observed Ly α luminosities. We discuss different scenarios such as *in-situ* star formation in low luminosity galaxies or scattered Ly α emission from an extended Ly α halos around high luminosity galaxies as possible alternatively to explain the observed Ly α luminosity. If the bias estimated for the DLA population based on clustering analysis as well as our mass estimation from the stacked absorption lines are true then the second alternative will be favored.

ACKNOWLEDGMENTS

We are grateful to Vikram Khairi for providing the metagalactic UV background. RS, PN, and PPJ acknowledge the support from Indo-French Centre for the Promotion of Advanced Research (IFCPAR) under project number 5504–2.

Funding for the SDSS and SDSS-II has been provided by the Alfred P. Sloan Foundation, the Participating Institutions, the National Science Foundation, the U.S. Department of Energy, the National Aeronautics and Space Administration, the Japanese Monbukagakusho, the Max Planck Society, and the Higher Education Funding Council for England. The SDSS Web Site is <http://www.sdss.org/>. The SDSS is managed by the Astrophysical Research Consortium for the Participating Institutions. The Participating Institutions are the American Museum of Natural History, Astrophysical Institute Potsdam, University of Basel, University of Cambridge, Case Western Reserve University, University of Chicago, Drexel University, Fermilab, the Institute for Advanced Study, the Japan Participation Group, Johns Hopkins University, the Joint Institute for Nuclear Astrophysics, the Kavli Institute for Particle Astrophysics and Cosmology, the Korean Scientist Group, the Chinese Academy of Sciences (LAMOST), Los Alamos National Laboratory, the Max-Planck-Institute for Astronomy (MPIA), the Max-Planck-Institute for Astrophysics (MPA), New Mexico State University, Ohio State University, University of Pittsburgh, University of Portsmouth, Princeton University, the United States Naval Observatory, and the University of Washington.

REFERENCES

Ahn S.-H., Lee H.-W., Lee H. M., 2003, *MNRAS*, **340**, 863
 Alavi A., et al., 2014, *ApJ*, **780**, 143
 Barnes L. A., Haehnelt M. G., 2010, *MNRAS*, **403**, 870

Begum A., Chengalur J. N., Karachentsev I. D., Kaisin S. S., Sharina M. E., 2006, *MNRAS*, **365**, 1220
 Bird S., Haehnelt M., Neeleman M., Genel S., Vogelsberger M., Hernquist L., 2015, *MNRAS*, **447**, 1834
 Bolatto A. D., et al., 2011, *ApJ*, **741**, 12
 Bolton A. S., et al., 2012, *AJ*, **144**, 144
 Bouché N., Murphy M. T., Péroux C., Csabai I., Wild V., 2006, *MNRAS*, **371**, 495
 Bouché N., et al., 2012, *MNRAS*, **419**, 2
 Bunker A. J., Warren S. J., Clements D. L., Williger G. M., Hewett P. C., 1999, *MNRAS*, **309**, 875
 Cai Z., et al., 2014, *ApJ*, **793**, 139
 Chelouche D., Bowen D. V., 2010, *ApJ*, **722**, 1821
 Chen H.-W., Lanzetta K. M., 2003, *ApJ*, **597**, 706
 Christensen L., Noterdaeme P., Petitjean P., Ledoux C., Fynbo J. P. U., 2009, *A&A*, **505**, 1007
 Christensen L., Møller P., Fynbo J. P. U., Zafar T., 2014, *MNRAS*, **445**, 225
 Cormier D., et al., 2014, *A&A*, **564**, A121
 Dawson K. S., et al., 2013, *AJ*, **145**, 10
 Dijkstra M., 2014, *PASA*, **31**, 40
 Dijkstra M., Kramer R., 2012, *MNRAS*, **424**, 1672
 Dijkstra M., Haiman Z., Spaans M., 2006, *ApJ*, **649**, 14
 Ekta B., Chengalur J. N., 2010, *MNRAS*, **406**, 1238
 Erb D. K., et al., 2014, *ApJ*, **795**, 33
 Feldmeier J. J., et al., 2013, *ApJ*, **776**, 75
 Filho M. E., et al., 2013, *A&A*, **558**, A18
 Filho M. E., Sánchez Almeida J., Amorín R., Muñoz-Tuñón C., Elmegreen B. G., Elmegreen D. M., 2016, *ApJ*, **820**, 109
 Font-Ribera A., et al., 2012, *J. Cosmology Astropart. Phys.*, **11**, 059
 Fox A. J., Ledoux C., Petitjean P., Srianand R., 2007, *A&A*, **473**, 791
 Frank S., Péroux C., 2010, *MNRAS*, **406**, 2235
 Fukugita M., Ménard B., 2015, *ApJ*, **799**, 195
 Fumagalli M., O’Meara J. M., Prochaska J. X., Kanekar N., 2010, *MNRAS*, **408**, 362
 Fumagalli M., O’Meara J. M., Prochaska J. X., Rafelski M., Kanekar N., 2015, *MNRAS*, **446**, 3178
 Fynbo J. P. U., et al., 2010a, *MNRAS*, **408**, 2128
 Fynbo J. P. U., et al., 2010b, *MNRAS*, **408**, 2128
 Fynbo J. P. U., et al., 2011, *MNRAS*, **413**, 2481
 Fynbo J. P. U., et al., 2013, *MNRAS*, **436**, 361
 Garel T., Blaizot J., Guiderdoni B., Michel-Dansac L., Hayes M., Verhamme A., 2015, *MNRAS*, **450**, 1279
 Ge J., Bechtold J., 1997, *ApJ*, **477**, L73
 Gronke M., Dijkstra M., 2016, *ApJ*, **826**, 14
 Hansen M., Oh S. P., 2006, *MNRAS*, **367**, 979
 Hartoog O. E., Fynbo J. P. U., Kaper L., De Cia A., Bagdonaite J., 2015, *MNRAS*, **447**, 2738
 Hashimoto T., et al., 2015, *ApJ*, **812**, 157
 Hathi N. P., Jansen R. A., Windhorst R. A., Cohen S. H., Keel W. C., Corbin M. R., Ryan Jr. R. E., 2008, *AJ*, **135**, 156
 Hayashino T., et al., 2004, *AJ*, **128**, 2073
 Hayes M., et al., 2010, *Nature*, **464**, 562
 Jeesson-Daniel A., Ciardi B., Maio U., Pierleoni M., Dijkstra M., Maselli A., 2012, *MNRAS*, **424**, 2193
 Jenkins E. B., 1986, *ApJ*, **304**, 739
 Jorgenson R. A., Wolfe A. M., 2014, *ApJ*, **785**, 16
 Jorgenson R. A., Murphy M. T., Thompson R., 2013, *MNRAS*, **435**, 482
 Kaplan K. F., Prochaska J. X., Herbert-Fort S., Ellison S. L., Dessauges-Zavadsky M., 2010, *PASP*, **122**, 619
 Kashikawa N., Misawa T., Minowa Y., Okoshi K., Hattori T., Toshikawa J., Ishikawa S., Onoue M., 2014, *ApJ*, **780**, 116
 Kennicutt Jr. R. C., 1998a, *ARA&A*, **36**, 189
 Kennicutt Jr. R. C., 1998b, *ApJ*, **498**, 541
 Kennicutt R. C., Evans N. J., 2012, *ARA&A*, **50**, 531

- Khaire V., Srianand R., 2015a, *MNRAS*, **451**, L30
- Khaire V., Srianand R., 2015b, *ApJ*, **805**, 33
- Khaire V., Srianand R., Choudhury T. R., Gaikwad P., 2016, *MNRAS*, **457**, 4051
- Khare P., vanden Berk D., York D. G., Lundgren B., Kulkarni V. P., 2012, *MNRAS*, **419**, 1028
- Krogager J.-K., Fynbo J. P. U., Møller P., Ledoux C., Noterdaeme P., Christensen L., Milvang-Jensen B., Sparre M., 2012, *MNRAS*, **424**, L1
- Krogager J.-K., et al., 2013, *MNRAS*, **433**, 3091
- Kulas K. R., Shapley A. E., Kollmeier J. A., Zheng Z., Steidel C. C., Hainline K. N., 2012, *ApJ*, **745**, 33
- Kulkarni V. P., Hill J. M., Schneider G., Weymann R. J., Storrie-Lombardi L. J., Rieke M. J., Thompson R. I., Jannuzi B. T., 2000, *ApJ*, **536**, 36
- Kulkarni V. P., Meiring J., Som D., Péroux C., York D. G., Khare P., Lauroesch J. T., 2012, *ApJ*, **749**, 176
- Laursen P., Sommer-Larsen J., 2007, *ApJ*, **657**, L69
- Ledoux C., Petitjean P., Bergeron J., Wampler E. J., Srianand R., 1998, *A&A*, **337**, 51
- Ledoux C., Petitjean P., Srianand R., 2003, *MNRAS*, **346**, 209
- Ledoux C., Petitjean P., Fynbo J. P. U., Møller P., Srianand R., 2006, *A&A*, **457**, 71
- López G., Chen H.-W., 2012, *MNRAS*, **419**, 3553
- Lowenthal J. D., Hogan C. J., Green R. F., Woodgate B., Caulet A., Brown L., Bechtold J., 1995, *ApJ*, **451**, 484
- Matsuda Y., et al., 2012, *MNRAS*, **425**, 878
- Ménard B., Wild V., Nestor D., Quider A., Zibetti S., Rao S., Turnshek D., 2011, *MNRAS*, **417**, 801
- Møller P., Warren S. J., 1993, *A&A*, **270**, 43
- Møller P., Warren S. J., Fall S. M., Fynbo J. U., Jakobsen P., 2002, *ApJ*, **574**, 51
- Møller P., Fynbo J. P. U., Fall S. M., 2004, *A&A*, **422**, L33
- Momose R., et al., 2014, *MNRAS*, **442**, 110
- Momose R., et al., 2016, *MNRAS*, **457**, 2318
- Murphy M. T., Bernet M. L., 2016, *MNRAS*, **455**, 1043
- Neeleman M., Wolfe A. M., Prochaska J. X., Rafelski M., 2013, *ApJ*, **769**, 54
- Neufeld D. A., 1990, *ApJ*, **350**, 216
- Neufeld D. A., 1991, *ApJ*, **370**, L85
- Noterdaeme P., Ledoux C., Petitjean P., Srianand R., 2008, *A&A*, **481**, 327
- Noterdaeme P., Petitjean P., Ledoux C., Srianand R., 2009, *A&A*, **505**, 1087
- Noterdaeme P., Srianand R., Mohan V., 2010, *MNRAS*, **403**, 906
- Noterdaeme P., et al., 2012a, *A&A*, **540**, A63
- Noterdaeme P., et al., 2012b, *A&A*, **547**, L1
- Noterdaeme P., Petitjean P., Pâris I., Cai Z., Finley H., Ge J., Pieri M. M., York D. G., 2014, *A&A*, **566**, A24
- Noterdaeme P., Petitjean P., Srianand R., 2015, *A&A*, **578**, L5
- O'Meara J. M., Chen H.-W., Kaplan D. L., 2006, *ApJ*, **642**, L9
- Osterbrock D. E., Ferland G. J., 2006, *Astrophysics of gaseous nebulae and active galactic nuclei*
- Ouchi M., et al., 2008, *ApJS*, **176**, 301
- Patra N. N., Chengalur J. N., Begum A., 2013, *MNRAS*, **429**, 1596
- Péroux C., Bouché N., Kulkarni V. P., York D. G., Vladilo G., 2011, *MNRAS*, **410**, 2251
- Pettini M., Smith L. J., Hunstead R. W., King D. L., 1994, *ApJ*, **426**, 79
- Prochaska J. X., Wolfe A. M., 2009, *ApJ*, **696**, 1543
- Prochaska J. X., Chen H.-W., Wolfe A. M., Dessauges-Zavadsky M., Bloom J. S., 2008, *ApJ*, **672**, 59
- Rafelski M., Wolfe A. M., Chen H.-W., 2011, *ApJ*, **736**, 48
- Rafelski M., Wolfe A. M., Prochaska J. X., Neeleman M., Mendez A. J., 2012, *ApJ*, **755**, 89
- Rahmani H., Srianand R., Noterdaeme P., Petitjean P., 2010, *MNRAS*, **409**, L59
- Rao S. M., Nestor D. B., Turnshek D. A., Lane W. M., Monier E. M., Bergeron J., 2003, *ApJ*, **595**, 94
- Rao S. M., Belfort-Mihalyi M., Turnshek D. A., Monier E. M., Nestor D. B., Quider A., 2011, *MNRAS*, **416**, 1215
- Rauch M., et al., 2008, *ApJ*, **681**, 856
- Reddy N. A., Steidel C. C., 2009, *ApJ*, **692**, 778
- Roychowdhury S., Chengalur J. N., Kaisin S. S., Karachentsev I. D., 2014, *MNRAS*, **445**, 1392
- Rubin K. H. R., Hennawi J. F., Prochaska J. X., Simcoe R. A., Myers A., Lau M. W., 2015, *ApJ*, **808**, 38
- Sánchez Almeida J., Elmegreen B. G., Muñoz-Tuñón C., Elmegreen D. M., 2014, *A&A Rev.*, **22**, 71
- Sardane G. M., Turnshek D. A., Rao S. M., 2015, *MNRAS*, **452**, 3192
- Schaerer D., Hayes M., Verhamme A., Teyssier R., 2011, *A&A*, **531**, A12
- Shapley A. E., Steidel C. C., Pettini M., Adelberger K. L., 2003, *ApJ*, **588**, 65
- Shi Y., Armus L., Helou G., Stierwalt S., Gao Y., Wang J., Zhang Z.-Y., Gu Q., 2014, *Nature*, **514**, 335
- Shibuya T., et al., 2014, *ApJ*, **788**, 74
- Shibuya T., Ouchi M., Harikane Y., 2015, *ApJS*, **219**, 15
- Shull J. M., Danforth C. W., Tilton E. M., 2014, *ApJ*, **796**, 49
- Song M., et al., 2014, *ApJ*, **791**, 3
- Srianand R., Petitjean P., Ledoux C., Ferland G., Shaw G., 2005, *MNRAS*, **362**, 549
- Srianand R., Hussain T., Noterdaeme P., Petitjean P., Krühler T., Japelj J., Pâris I., Kashikawa N., 2016, *MNRAS*, **460**, 634
- Steidel C. C., Hamilton D., 1992, *AJ*, **104**, 941
- Steidel C. C., Adelberger K. L., Shapley A. E., Pettini M., Dickinson M., Giavalisco M., 2003, *ApJ*, **592**, 728
- Steidel C. C., Erb D. K., Shapley A. E., Pettini M., Reddy N., Bogosavljević M., Rudie G. C., Rakic O., 2010, *ApJ*, **717**, 289
- Steidel C. C., Bogosavljević M., Shapley A. E., Kollmeier J. A., Reddy N. A., Erb D. K., Pettini M., 2011, *ApJ*, **736**, 160
- Straka L. A., et al., 2015, *MNRAS*, **447**, 3856
- Toribio M. C., Solanes J. M., Giovanelli R., Haynes M. P., Martin A. M., 2011, *ApJ*, **732**, 93
- Trainor R. F., Steidel C. C., Strom A. L., Rudie G. C., 2015, *ApJ*, **809**, 89
- Vasei K., et al., 2016, preprint, ([arXiv:1603.02309](https://arxiv.org/abs/1603.02309))
- Verhamme A., Schaerer D., Maselli A., 2006, *A&A*, **460**, 397
- Verhamme A., Dubois Y., Blaizot J., Garel T., Bacon R., Devriendt J., Guiderdoni B., Slyz A., 2012, *A&A*, **546**, A111
- Vladilo G., Prochaska J. X., Wolfe A. M., 2008, *A&A*, **478**, 701
- Wild V., Hewett P. C., Pettini M., 2007, *MNRAS*, **374**, 292
- Wolfe A. M., Prochaska J. X., 2000, *ApJ*, **545**, 603
- Wolfe A. M., Prochaska J. X., Gawiser E., 2003a, *ApJ*, **593**, 215
- Wolfe A. M., Gawiser E., Prochaska J. X., 2003b, *ApJ*, **593**, 235
- Wolfe A. M., Gawiser E., Prochaska J. X., 2005, *ARA&A*, **43**, 861
- Wyder T. K., et al., 2009, *ApJ*, **696**, 1834
- Yamada T., Matsuda Y., Kousai K., Hayashino T., Morimoto N., Umemura M., 2012, *ApJ*, **751**, 29
- York D. G., et al., 2006, *MNRAS*, **367**, 945
- Zheng Z., Miralda-Escudé J., 2002, *ApJ*, **578**, 33
- Zheng Z., Cen R., Weinberg D., Trac H., Miralda-Escudé J., 2011, *ApJ*, **739**, 62
- Zwaan M. A., van der Hulst J. M., Briggs F. H., Verheijen M. A. W., Ryan-Weber E. V., 2005, *MNRAS*, **364**, 1467

APPENDIX A:

A1 Dependence on QSOs colour :

Here, we present the dependence of Ly α emission on background QSOs colour by considering the $CNR \geq 4$ systems. The results are shown in Fig. A3 and measured luminosities

are summarized in Table A2 in the Appendix. The double hump profile is clearly visible even in this case that has ~ 30 per cent more systems. However, the total luminosity measured in the median stacked spectrum, $(19.1 \pm 6.6) \times 10^{40}$ erg s $^{-1}$, is slightly less but consistent within 0.4σ level to what we measure for $CNR \geq 5$. The double Gaussian fits are shown in Fig. A3. It is also clear from Table A2 that derived luminosities using Gaussian fits to the blue and red hump are significant at more than 3.3σ level. Here also we find L_{λ}^r being higher than L_{λ}^b . However, the excess is less than what we have seen in the $CNR \geq 5$ sample. The measured velocity shifts of Gaussian peaks with respect to the central wavelength systemic redshift are consistent with that measured for the $CNR \geq 5$ case. *This enlarged sample also shows : (i) the presence of enhanced emission in the blue part; (ii) the blue peak having more velocity shift with respect to the systemic redshift compared to the red and (iii) L_{λ}^r being higher than L_{λ}^b for systems with $(r - i) < 0.05$.*

In addition, the trend of total luminosity being nearly same, and the double hump present only in low $(r - i)$ subsamples, as seen in Fig. 6, is also present when we consider systems with $CNR \geq 4$. However, the average luminosities are slightly less from what we find for $CNR \geq 5$ sample.

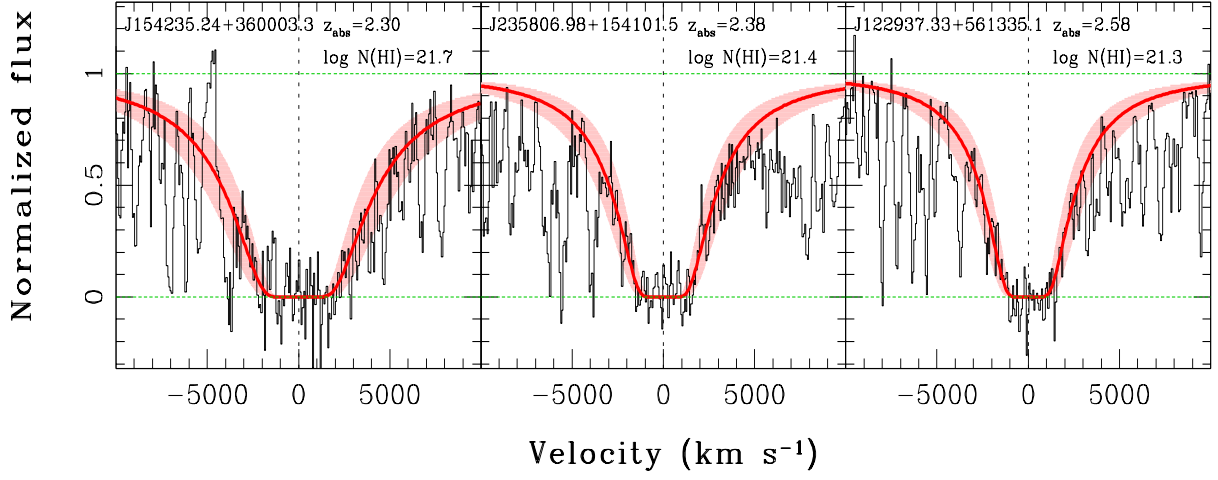


Figure A1. Examples of DLAs from our parent sample with large pixel-to-pixel variation in the absorption trough (see also, Section 3.1)

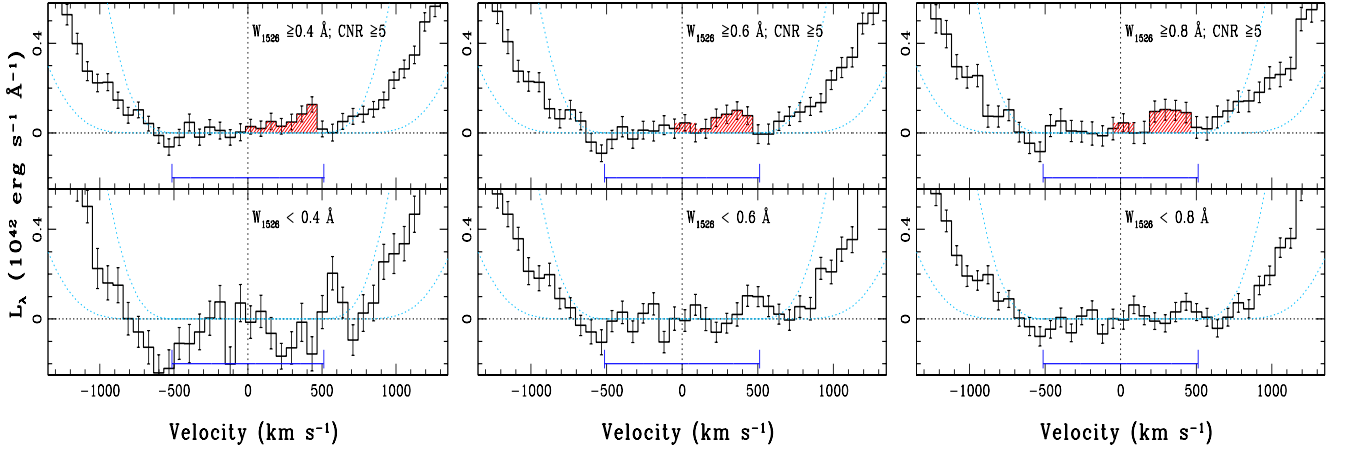


Figure A2. Left to right : Comparison of median stacked spectrum for a sub-sample with $CNR \geq 5$ and W_{1526} greater than (top panel) and less than (bottom panels) 0.4, 0.6 and 0.8 Å, respectively. The blue segment shows the DLA core with $\tau \geq 10$ for $\log N(\text{H I}) = 21.0$. The dashed curves show the synthetic profiles for lower (i.e., $\log N(\text{H I}) = 21$) and median (i.e., $\log N(\text{H I}) = 21.23$) column density of DLAs used to get the stacked spectrum.

Table A1. Luminosity of Ly α line in bootstrap analysis of median stacked spectra for various sub-samples based on W_{1526} and CNR limit of ≥ 5 and ≥ 4 .

sample criteria	number	Ly α luminosity ($\times 10^{40} \text{ erg s}^{-1}$)		
		DLA-bottom	median stack L_{λ}^b	L_{λ}^r
$W_{1526} \geq 0.4 \text{ \AA}$ and $CNR \geq 5$	513	13.49 ± 4.05	1.16 ± 2.84	12.34 ± 2.90
$W_{1526} < 0.4 \text{ \AA}$ and $CNR \geq 5$	112	-26.27 ± 8.33	-10.78 ± 5.92	-15.45 ± 5.85
$W_{1526} \geq 0.6 \text{ \AA}$ and $CNR \geq 5$	391	13.76 ± 4.69	1.70 ± 3.00	12.05 ± 3.33
$W_{1526} < 0.6 \text{ \AA}$ and $CNR \geq 5$	279	3.41 ± 5.44	-1.43 ± 3.76	4.85 ± 3.93
$W_{1526} \geq 0.4 \text{ \AA}$ and $CNR \geq 4^a$	627	11.05 ± 3.67	2.02 ± 1.65	11.48 ± 1.75
$W_{1526} < 0.4 \text{ \AA}$ and $CNR \geq 4$	119	-28.18 ± 8.09	-11.60 ± 5.78	-16.59 ± 5.66
$W_{1526} \geq 0.6 \text{ \AA}$ and $CNR \geq 4$	496	9.92 ± 4.18	-0.43 ± 2.93	10.34 ± 2.98
$W_{1526} < 0.6 \text{ \AA}$ and $CNR \geq 4$	320	1.87 ± 5.00	-2.90 ± 3.47	4.77 ± 3.60
$W_{1526} \geq 0.8 \text{ \AA}$ and $CNR \geq 4$	370	8.72 ± 4.78	-0.80 ± 3.36	9.52 ± 3.40
$W_{1526} < 0.8 \text{ \AA}$ and $CNR \geq 4$	511	-0.04 ± 4.03	-4.07 ± 2.80	4.03 ± 2.91

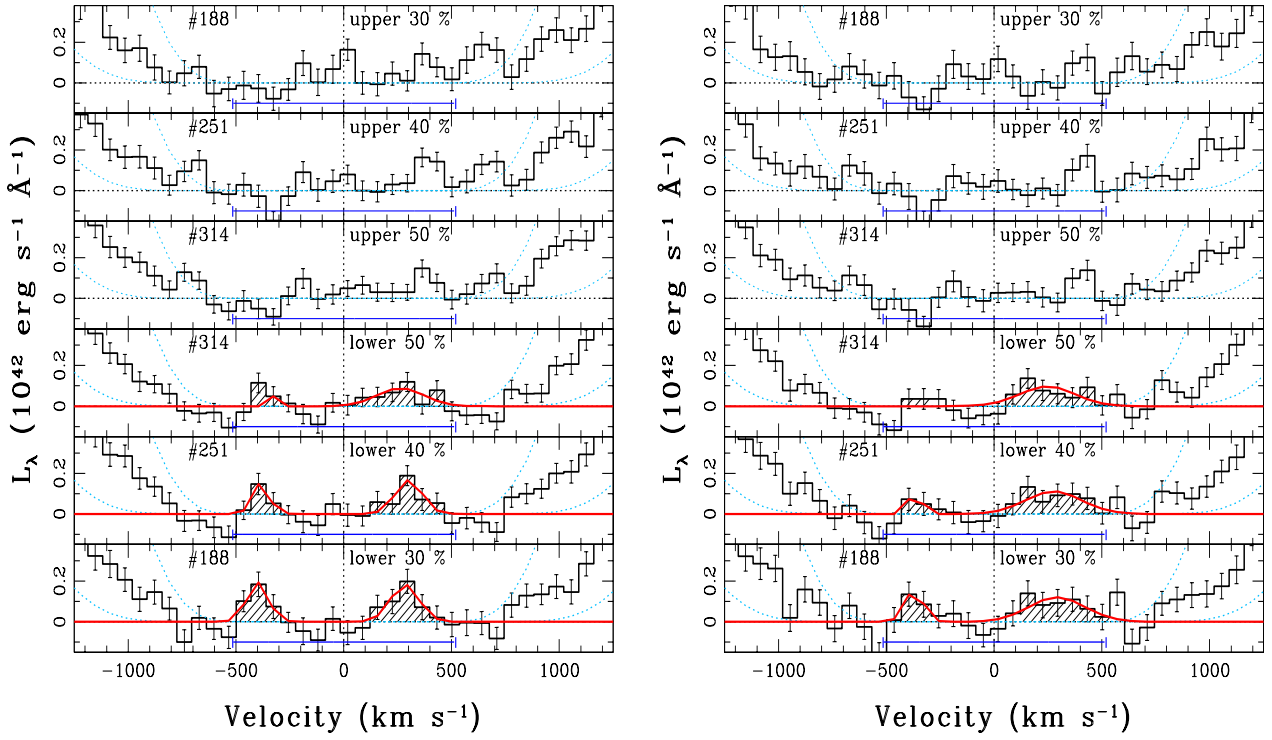


Figure A3. Same as Fig. 6, for the sub-sample with relaxed CNR limit to $\text{CNR} \geq 4$.

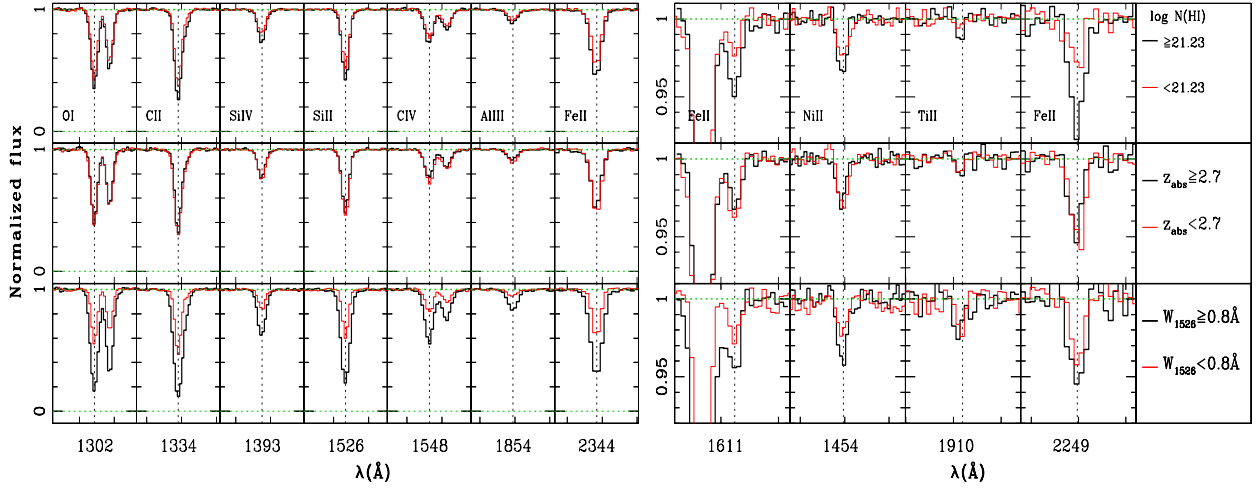


Figure A4. Comparison of several absorption lines in the composite spectra of a number of sub-samples, defined in Table 2. Each row shows different lines in the composite spectra of the same two sub-samples (one in red and the other in black), which are detailed in the last column of each row. Each column contains lines of the same species, indicated in the top row of that column, the wavelength of which is indicated below each column.

Table A2. Same as Table 4, after relaxing the *CNR* limit to $CNR \geq 4$.

Sample	$(r - i)$	$\langle \Delta(r - i) \rangle$	Ly α luminosity ($\times 10^{40} \text{ erg s}^{-1}$)			velocity-offset		FWHM (km s^{-1})
			DLA-bottom	L_{λ}^b	L_{λ}^r	Δv^r	Δv^b	
lower 30%	< 0.04	-0.08	19.07 ± 6.61	7.65 ± 4.42	11.41 ± 4.92	283 ± 24	-401 ± 19	—
lower 40%	< 0.07	-0.06	13.07 ± 5.84	3.92 ± 3.94	9.15 ± 4.31	301 ± 22	-383 ± 24	—
lower 50%	< 0.10	-0.04	10.47 ± 5.24	0.95 ± 3.51	9.52 ± 3.89	263 ± 48	-336 ± 54	205 ± 112
upper 50%	> 0.10	0.12	10.87 ± 5.10	-0.65 ± 3.66	11.52 ± 3.56	—	—	—
upper 40%	> 0.13	0.13	13.27 ± 5.64	-1.10 ± 4.05	14.37 ± 3.93	—	—	—
upper 30%	> 0.16	0.16	10.77 ± 6.69	-0.38 ± 4.93	11.15 ± 4.52	—	—	—

Table A3. Equivalent widths of metal absorption lines for various sub-samples.

Transition	All		W_{1526}		$W_r(\text{\AA})$		$\log N(\text{H I})$		z_{abs}
	(S1)	$\geq 0.8 \text{ \AA}$ (S2)	$< 0.8 \text{ \AA}$ (S3)	$\geq 0.4 \text{ \AA}$ (S4)	≥ 21.23 (S5)	< 21.23 (S6)	≥ 2.7 (S7)	< 2.7 (S8)	
Al II $\lambda 1670$	0.732 ± 0.008	1.218 ± 0.012	0.483 ± 0.008	0.864 ± 0.009	0.841 ± 0.012	0.589 ± 0.011	0.713 ± 0.011	0.735 ± 0.012	
Al III $\lambda 1854$	0.171 ± 0.006	0.332 ± 0.009	0.092 ± 0.007	0.219 ± 0.007	0.200 ± 0.008	0.153 ± 0.008	0.161 ± 0.009	0.175 ± 0.008	
Al III $\lambda 1862$	0.103 ± 0.006	0.192 ± 0.009	0.050 ± 0.007	0.135 ± 0.006	0.134 ± 0.008	0.079 ± 0.008	0.084 ± 0.009	0.105 ± 0.007	
Co II $\lambda 1466$	0.009 ± 0.003	0.022 ± 0.004	0.002 ± 0.004	0.012 ± 0.003	0.007 ± 0.004	0.002 ± 0.004	0.011 ± 0.005	0.008 ± 0.003	
Cr II $\lambda 2056$	0.085 ± 0.007	0.142 ± 0.010	0.060 ± 0.009	0.077 ± 0.007	0.087 ± 0.009	0.038 ± 0.010	0.056 ± 0.012	0.093 ± 0.007	
Cr II $\lambda 2066$	0.043 ± 0.006	0.089 ± 0.009	0.048 ± 0.008	0.047 ± 0.007	0.032 ± 0.008	0.039 ± 0.009	0.043 ± 0.010	0.054 ± 0.007	
C II $\lambda 1334$	0.934 ± 0.010	1.513 ± 0.015	0.644 ± 0.011	1.167 ± 0.012	1.094 ± 0.015	0.812 ± 0.014	0.866 ± 0.015	0.977 ± 0.014	
C IV $\lambda 1548$	0.362 ± 0.007	0.676 ± 0.012	0.253 ± 0.007	0.508 ± 0.008	0.399 ± 0.009	0.367 ± 0.010	0.321 ± 0.010	0.420 ± 0.009	
C IV $\lambda 1550$	0.228 ± 0.006	0.403 ± 0.011	0.171 ± 0.007	0.305 ± 0.007	0.247 ± 0.008	0.234 ± 0.009	0.175 ± 0.009	0.264 ± 0.008	
Fe II $\lambda 1608$	0.456 ± 0.006	0.750 ± 0.010	0.293 ± 0.007	0.569 ± 0.007	0.534 ± 0.009	0.411 ± 0.008	0.432 ± 0.009	0.494 ± 0.009	
Fe II $\lambda 1611$	0.048 ± 0.004	0.070 ± 0.005	0.028 ± 0.005	0.056 ± 0.004	0.078 ± 0.005	0.025 ± 0.005	0.040 ± 0.005	0.050 ± 0.005	
Fe II $\lambda 2249$	0.072 ± 0.010	0.164 ± 0.015	0.062 ± 0.014	0.105 ± 0.011	0.158 ± 0.014	0.053 ± 0.015	0.094 ± 0.018	0.102 ± 0.011	
Fe II $\lambda 2260$	0.089 ± 0.009	0.156 ± 0.014	0.078 ± 0.012	0.110 ± 0.010	0.132 ± 0.013	0.080 ± 0.013	0.076 ± 0.017	0.124 ± 0.010	
Fe II $\lambda 2344$	0.894 ± 0.023	1.471 ± 0.029	0.578 ± 0.030	1.152 ± 0.022	1.083 ± 0.031	0.819 ± 0.030	0.886 ± 0.045	0.891 ± 0.019	
Fe II $\lambda 2374$	0.605 ± 0.020	0.988 ± 0.028	0.427 ± 0.026	0.704 ± 0.022	0.744 ± 0.029	0.477 ± 0.027	0.565 ± 0.041	0.622 ± 0.018	
Fe II $\lambda 2382$	1.221 ± 0.021	1.902 ± 0.030	0.894 ± 0.026	1.384 ± 0.024	1.329 ± 0.030	1.075 ± 0.030	1.142 ± 0.043	1.223 ± 0.020	
Fe II $\lambda 2586$	0.791 ± 0.041	1.363 ± 0.061	0.532 ± 0.047	1.038 ± 0.043	0.913 ± 0.053	0.706 ± 0.058	0.587 ± 0.120	0.856 ± 0.030	
Fe II $\lambda 2600$	1.186 ± 0.042	1.895 ± 0.059	0.778 ± 0.051	1.448 ± 0.042	1.353 ± 0.053	1.069 ± 0.062	0.998 ± 0.127	1.265 ± 0.032	
Mg II $\lambda 2796$	1.901 ± 0.086	2.954 ± 0.111	1.267 ± 0.116	2.184 ± 0.084	2.188 ± 0.098	1.689 ± 0.134	— \pm —	1.904 ± 0.084	
Mg II $\lambda 2803$	1.813 ± 0.105	2.858 ± 0.140	1.123 ± 0.104	2.107 ± 0.094	2.010 ± 0.097	1.716 ± 0.150	— \pm —	1.828 ± 0.105	
Mg I $\lambda 2852$	0.418 ± 0.075	0.712 ± 0.100	0.254 ± 0.112	0.586 ± 0.083	0.560 ± 0.103	0.326 ± 0.105	— \pm —	0.416 ± 0.076	
Mn II $\lambda 2576$	0.142 ± 0.033	0.169 ± 0.054	0.121 ± 0.032	0.157 ± 0.037	0.176 ± 0.029	0.107 ± 0.062	0.064 ± 0.103	0.155 ± 0.018	
Mn II $\lambda 2594$	0.057 ± 0.031	0.105 ± 0.052	0.049 ± 0.034	0.115 ± 0.035	0.108 ± 0.039	0.037 ± 0.042	0.010 ± 0.103	0.093 ± 0.018	
Mn II $\lambda 2606$	0.032 ± 0.026	0.083 ± 0.039	0.010 ± 0.033	0.061 ± 0.028	0.096 ± 0.036	0.010 ± 0.036	0.021 ± 0.084	0.055 ± 0.018	
Ni II $\lambda 1317$	0.131 ± 0.009	0.209 ± 0.015	0.096 ± 0.011	0.121 ± 0.011	0.123 ± 0.012	0.111 ± 0.013	0.109 ± 0.013	0.157 ± 0.012	
Ni II $\lambda 1370$	0.057 ± 0.005	0.078 ± 0.008	0.034 ± 0.007	0.083 ± 0.006	0.105 ± 0.007	0.012 ± 0.007	0.056 ± 0.007	0.078 ± 0.008	
Ni II $\lambda 1454$	0.029 ± 0.003	0.049 ± 0.005	0.027 ± 0.004	0.044 ± 0.004	0.039 ± 0.005	0.026 ± 0.005	0.034 ± 0.005	0.031 ± 0.004	
Ni II $\lambda 1467$	0.024 ± 0.003	0.055 ± 0.005	0.009 ± 0.004	0.039 ± 0.004	0.025 ± 0.005	0.014 ± 0.005	0.031 ± 0.005	0.026 ± 0.004	
Ni II $\lambda 1709$	0.059 ± 0.004	0.095 ± 0.007	0.036 ± 0.006	0.083 ± 0.005	0.087 ± 0.006	0.039 ± 0.006	0.038 ± 0.006	0.073 ± 0.006	
Ni II $\lambda 1741$	0.079 ± 0.005	0.144 ± 0.008	0.054 ± 0.007	0.101 ± 0.006	0.111 ± 0.007	0.035 ± 0.007	0.070 ± 0.007	0.078 ± 0.007	
Ni II $\lambda 1751$	0.063 ± 0.005	0.069 ± 0.007	0.031 ± 0.006	0.067 ± 0.005	0.072 ± 0.006	0.023 ± 0.007	0.059 ± 0.006	0.034 ± 0.007	
O I $\lambda 1302$	0.732 ± 0.009	1.186 ± 0.013	0.457 ± 0.011	0.903 ± 0.010	0.794 ± 0.013	0.669 ± 0.013	0.715 ± 0.013	0.724 ± 0.013	
Si II $\lambda 1304$	0.546 ± 0.009	0.930 ± 0.014	0.341 ± 0.012	0.649 ± 0.011	0.592 ± 0.014	0.520 ± 0.013	0.531 ± 0.014	0.540 ± 0.013	
Si II $\lambda 1526$	0.674 ± 0.007	1.206 ± 0.010	0.427 ± 0.007	0.846 ± 0.008	0.752 ± 0.010	0.606 ± 0.010	0.649 ± 0.011	0.694 ± 0.010	
Si II $\lambda 1808$	0.141 ± 0.006	0.262 ± 0.009	0.090 ± 0.007	0.207 ± 0.006	0.221 ± 0.008	0.100 ± 0.008	0.142 ± 0.008	0.159 ± 0.008	
Si IV $\lambda 1393$	0.321 ± 0.006	0.543 ± 0.010	0.208 ± 0.007	0.373 ± 0.007	0.342 ± 0.009	0.268 ± 0.008	0.312 ± 0.009	0.331 ± 0.008	
Si IV $\lambda 1402$	0.169 ± 0.005	0.356 ± 0.008	0.120 ± 0.006	0.231 ± 0.006	0.190 ± 0.007	0.158 ± 0.007	0.183 ± 0.007	0.204 ± 0.007	
Ti II $\lambda 1910$	0.021 ± 0.005	0.039 ± 0.007	0.015 ± 0.006	0.037 ± 0.005	0.030 ± 0.007	0.011 ± 0.007	0.015 ± 0.008	0.017 ± 0.006	
Zn II+Mg I $\lambda 2026$	0.111 ± 0.007	0.179 ± 0.010	0.057 ± 0.008	0.120 ± 0.008	0.137 ± 0.010	0.070 ± 0.009	0.082 ± 0.011	0.097 ± 0.008	
Zn II+Cr II $\lambda 2062$	0.102 ± 0.006	0.189 ± 0.010	0.079 ± 0.008	0.123 ± 0.007	0.116 ± 0.009	0.061 ± 0.009	0.079 ± 0.011	0.129 ± 0.007	